Particle identification at the LHC

D. Fournier

LAL 07-06
January 2007

Particle Identification at the LHC

Daniel Fournier

LAL, Univ Paris-Sud, IN2P3/CNRS, Orsay, France

Lectures given at the XXXIV International Meeting on Fundamental Physics **"IMFP2006"**,
From HERA and the TeVatron to the LHC
April 2-7, 2006 - El Escorial, Madrid, Spain

An extended version was also given in the framework of the CERN Academic training (2004)

U.M.R
de
l'Université Paris-Sud

Institut National de
Physique Nucléaire et de
Physique des Particules du CNRS

LAL ~ Bât. 200 ~ B.P. 34 ~ 91898 Orsay Cedex ~ France

LAL 07-06
January 2007

Particle Identification at the LHC

Daniel Fournier

LAL, Univ Paris-Sud, IN2P3/CNRS, Orsay, France

Abstract

After an introduction on hadron identification in ALICE and LHCb, the presentation concentrates on particle identification and measurement in the context of high p_T reactions in ATLAS and CMS. Muons, electrons, photons, tau leptons,... are considered, both at the trigger and at the analysis levels. The role of identification is illustrated in some key physics channels (Higgs search,...)

Contents

1 Introduction

1.1 Some LHC parameters

Before starting a detailed discussion on particle identification, it is worthwhile recalling the main parameters of the collider[1] which determine the conditions of experimentation at the interaction points:

Table 1: LHC parameters.

Nominal settings	
Beam energy (TeV)	7.0
Number of particles per bunch	1.15 10^{11}
Number of bunches per beam	**2808**
Crossing angle (μrad)	**285**
Norm transverse emittance (μm rad)	3.75
Bunch length (cm)	7.55
Beta function at IP 1,2,5,8 (m)	**0,55**,10,**0.55**,10
Related parameters	
Luminosity in IP 1 & 5 (cm^{-2} s^{-1})	10^{34}
Luminosity in IP 2 & 8 (cm^{-2} s^{-1})	$\sim$5 10^{32}
Transverse beam size at IP 1 & 5 (μm)	16.7
Transverse beam size at IP 2 & 8 (μm)	70.9
Stored energy per beam (MJ)	**362**

When the machine is filled with the nominal number of bunches (2808 filled bunches and 756 empty ones), they collide every 25 ns and give rise, at the nominal current and high luminosity of 10^{34}cm^{-2}s^{-1}, to 23 inelastic collisions in average. The high luminosity requires a very strong focusing near the interaction points IP1 and IP5 with a β^* of 55 cm.

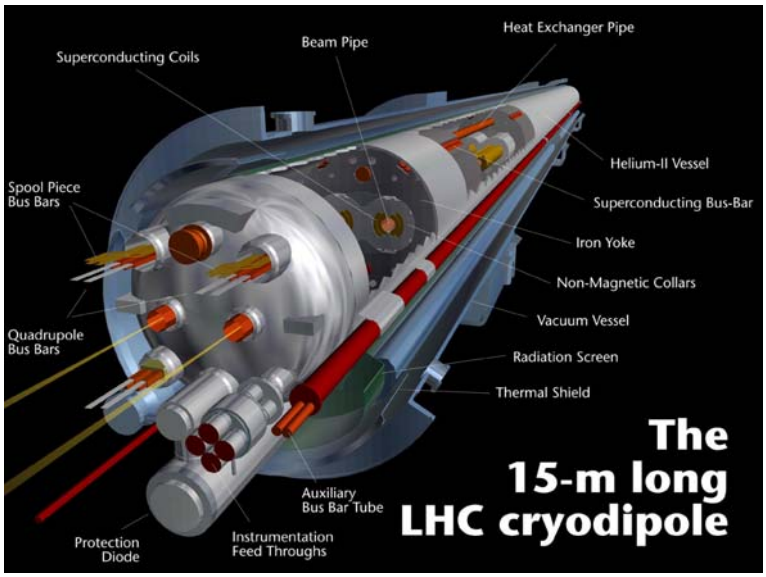

Figure 1: LHC dipoles.

On the contrary Alice (at IP2) in the proton-proton mode is aiming at a luminosity $L < 5 \times 10^{30}$ to cope with the specific features of the TPC (drift time of several tens of microseconds). This requires a β^* increased to 200 m, and/or transversally displaced beams.

In the Lead-Lead collision mode, for which Alice is specifically designed, the conditions are somewhat different: the energy in the center of mass system is $\sqrt{s}$ = 5.5 TeV/nucleon, instead of 14 TeV -due to the proton/neutron fraction in lead ions- and the reduced number of ion bunches (592) gives bunch collisions every 100 ns, keeping in mind that with a maximum of $\sim 10^8$ ions/bunch, β = 50 cm and $L = 10^{27}$ by far not all bunches give rise to an inelastic interaction. Light ions and p-ions collisions are also possible, and foreseen later.

LHCb (at IP8) is aiming at a maximum number of bunch collisions with one inelastic interaction only, which corresponds to $L \leq 2\ 10^{32}$. This requires β^* ~10 m for the nominal current giving high luminosity in IP1 and IP5.

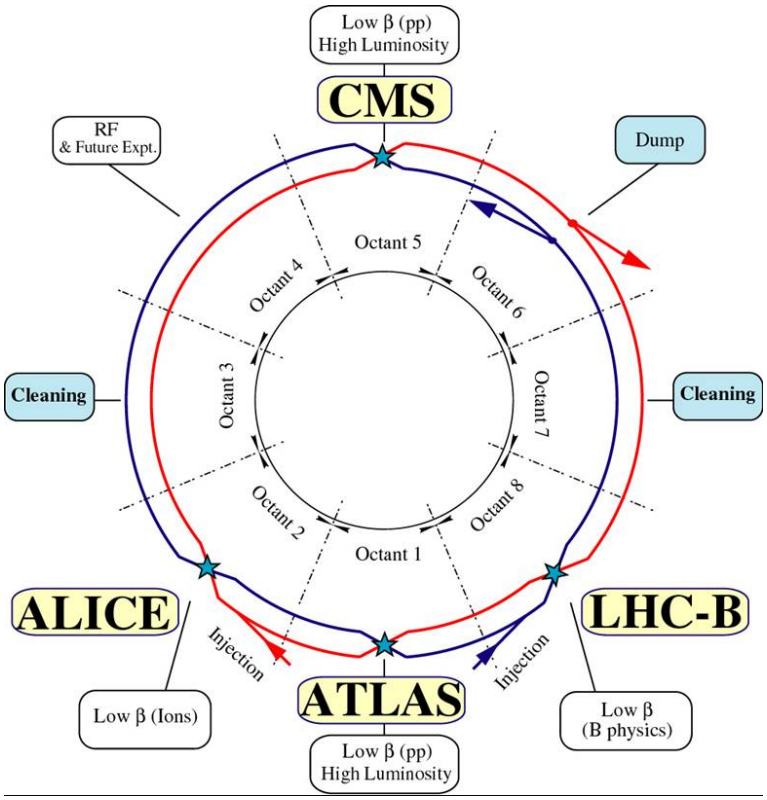

Figure 2: LHC schematic.

1.2 Some basic features of proton-proton collisions at $\sqrt{s}$ = 14 TeV

Extrapolating from present data (up to 1.96 TeV at the Tevatron) one estimates an inelastic, non-diffractive pp cross-section of about 70 mb at the energy of the LHC.

Among the inelastic events, it is worth noting at this point that:

- Different event generators, tuned with the present collider data predict a $B\bar{B}$ pairs production cross section of close to 1 mb, ie 1% of the inelastic events.
- The production cross section of W and Zs by weak processes increases fast with energy, but the production cross section of jets above a fixed transverse energy (E_T) increases even faster, due to the value of QCD couplings, and the shape of parton distribution functions (see below).

From this basic fact one expects larger signal statistics at the LHC as compared to the Tevatron, but often with a reduced signal/background ratio.

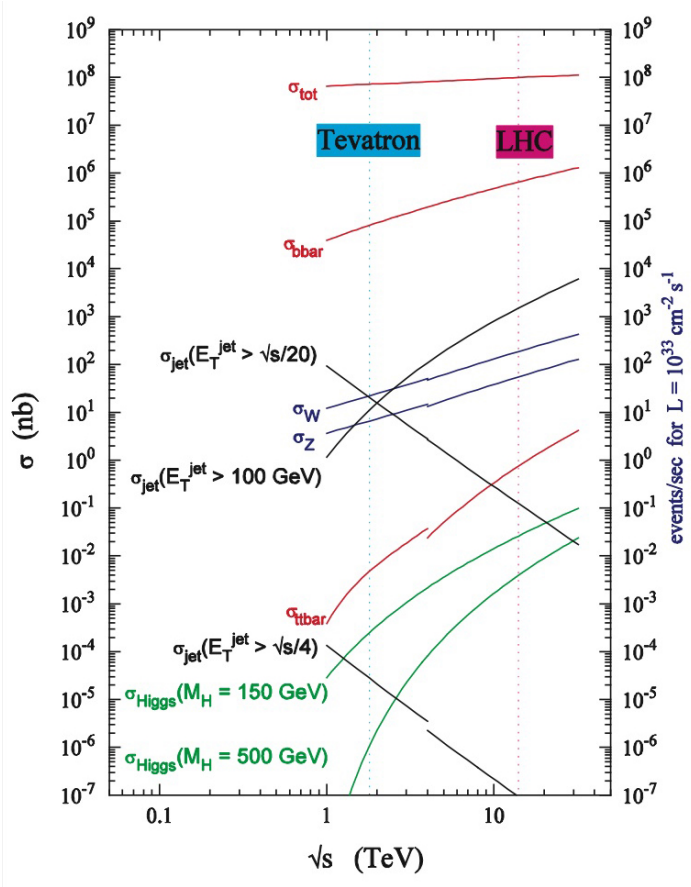

Figure 3: Cross-sections and rate at the LHC

1.3 Parton-parton collisions at $\sqrt{s} = 14$ TeV

Microscopic understanding of hard (ie with a large transverse momentum transfer to at least one particle of the final state) proton-proton collisions calls for a description in terms of collisions between parton constituents (quarks and gluons) of both projectiles. x_i being the fraction of momentum carried by parton "i" and with $\sqrt{S} = 14$ TeV

- the effective center of mass energy is $\sqrt{s} = 2\ x_1 x_2\ \sqrt{S}$
- the boost of the center of mass of the sub-process is $\sqrt{s} = (x_1\text{-}x_2)/(x_1+x_2)$

The non-interacting debris of the protons being lost in the forward/backward directions, only the transverse components p_x, p_y of the 4-momentum (E,p) conservation are useful ($p_T = \sqrt{(p_x^2 + p_y^2)}$).

The parton-parton luminosity is calculated from the parton distribution function f(x, Q^2) which is the probability to find a parton with the momentum fraction x in the proton.

Given the experimentally measured parton distributions (as an example distributions obtained by the CTEQ[2] collaboration are given in figure 4), gluon-gluon collisions dominate QCD processes as long as $x_1 x_2$ is not too large. Introducing $\tau = x_1 x_2$ one gets:

$$\tau dL/d\tau = \int \tau G(x, Q^2) G(\tau/x, Q^2) dx/x \qquad (1)$$

Because W and Z couple directly only to quarks, the gluon dominance does not apply to electroweak processes.

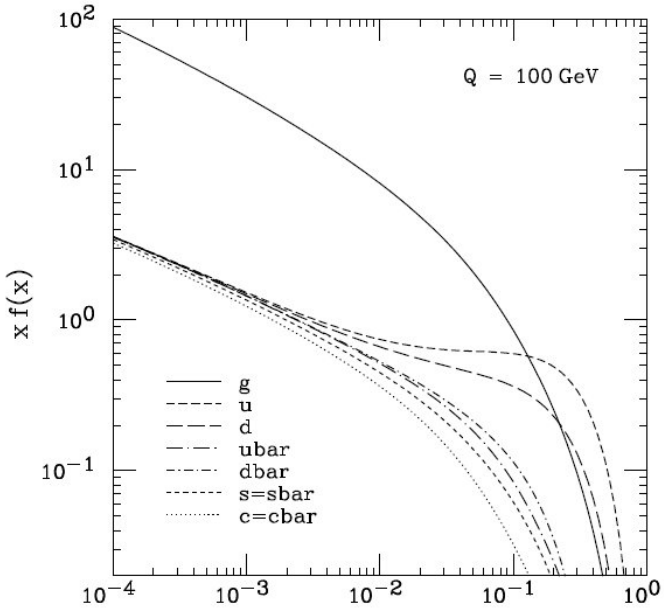

Figure 4: CTEQ6 parton distribution function.

1.4 Minimum bias events

Unlike hard collisions, most nucleon-nucleon collisions are peripheral. Soft particles (mostly pions) are produced with a quasi constant density in the "plateau" region ($\eta = \pm 5$) of the allowed ($\eta = \pm 10$) pseudo-rapidity interval at the LHC. Because they can be obtained by a random triggering of an experiment, these events are usually called "minimum bias" events. The pseudo-rapidity is defined by η = -log(tg(θ/2)) while the rapidity y is given by y = log(E+pz)/(E-pz)(cosθ = pz/p).

Despite accurate measurements at the Tevatron and below, there is still a rather large uncertainty on the height of the "rapidity plateau" expected at LHC (from ∼5 to ∼8 charged particle per η unit, depending on the model used for the extrapolation).

The average p_T of min bias charged particles (pions) is expected to be ∼0.7 GeV/c. From the invariance of strong interactions under strong isospin, there are as many neutral pions as positive, or negative pions produced. They appear as photons with half the transverse momentum of the parent π^0 in average. The description of minimum bias events from parton constituents of the protons requires non-perturbative calculations, not yet fully mastered -see below-.

1.5 "Particles" in hard collisions

Elementary constituents interact as such in "hard processes" namely: quarks and leptons as matter particles, and gluons and electroweak bosons (W, Z and photons) as gauge particles.

Particles with strong interactions, ie gluons and quarks materialize as "jets" (non perturbative aspect of QCD). Heavy quarks (c, b) can be signed by the finite life time and/or the leptonic decay of the mesons (or baryons) carrying their quantum number in the jet. The same kind of signatures (finite life time, leptonic decay) applies also to the τ leptons, of course without a surrounding jet. W and Z appear through their decay particles, either charged leptons or neutrinos, or quarks which once more materialize as jets.

In summary the relevant "particles" for hard collisions are high p_T leptons, high p_T jets, and missing momentum signing escaping neutrinos.

Those are the "building blocks" out of which, from triggering to final analysis is studied the physics of hard collisions, those allowing to reveal new processes (production of top quark, Higgs boson, supersymetric particles,...).

1.6 "Particles" in soft collisions

Below some p_T (a few GeV) the structure in jets is no longer visible. Soft gluons "conspire" to produce hadrons (π, K, ...) of the "minimum" bias events. In this regime of soft collisions the "particles" are pions, kaons, ... with in general intermediate hadronic resonances (ρ, ω, η, φ, ...).

Heavy quarks decay by W exchange (no FCNC) with CKM mixing, and appear finally as well as "groups" of pions, kaons,... with a fraction of events containing electrons or muons from the intermediate W in proportion of the leptonic couplings ($e\nu$ and $\mu\nu$: 10.6% each, hadrons: (ud, cs) 68.5%).

The long life time of hadrons carrying b, c (and s) quarks leads to visible path length which allows to sign them. The higher mass states (B-hadrons) generate furthermore distinctive p_T ($\sim$M/2$\sim$2.5 GeV) in their decay. Narrow resonances of heavy quarks (Ψ, Y, ...) are also interesting signatures, including in heavy ion collisions. In summary, for low p_T proton-proton physics the "particles" are pion, kaons, ... and their intermediate hadronic resonances.

When studying ion-ion collisions, many of the interesting phenomena are addressed by selecting central collisions (small impact parameter), as opposed to the peripheral ones in which a small fraction of the constituent nucleons participate, the others being spectator nucleons emitted at 0°.

At small impact parameter and high energy, the head-on collisions of nuclei generate a large number of soft gluons, which in turn materialise into hadrons. The expected density of gluons per pseudo-rapidity interval is $\sim$3000 when colliding lead ions at LHC

There is interest in understanding:

- in which conditions (energy density ϵ) this final sate evolves through an intermediate quark-gluon plasma (new state of matter, possibly already observed)
- how hard probes (Ψ, Y) behave when traversing such a medium
- how this medium "cools-down" to ordinary matter.

This last part is best studied with soft particles. Important observables are:

- the nature of produced hadrons (fraction of strange particules, ...)
- the transverse momentum spectrum
- the existence of intermediate states (resonances like $\phi \to K\bar{K}$), ...

In order to realize this program, ALICE is aiming at a 3 standard deviation separation between π, K, and p in the 0.1 GeV to "few GeV" range.

2 Particle identification in Alice and LHb

At LHC energies the Pb-Pb total cross section is 8 barns. At the maximum expected luminosity of L = $10^{27}\mathrm{cm}^{-2}\mathrm{s}^{-1}$ this corresponds to a rate of only 8 kHz. Thus the high multiplicity is the problem, not the rate. In these conditions the Time Projection chamber (TPC) is the choice detector, and Alice has built its detector around such a large TPC, inserted into the former L3 magnet at IP2[3].

2.1 The Alice time of flight system

For non relativistic particles the Time of Flight measurement is a powerful tool for particle identification. The momentum p being measured in the TPC and in the additional inner tracking system (ITS), several mass hypotheses are tested by comparing the measured time δT between the collision and the accurately timed signal in the dedicated TOF system ($\delta T = L/\beta c$, $\beta = p/\sqrt{(p^2 + m^2)}$).

The useful momentum range increases with the accuracy of measurement of δT and the flight length L.

The detectors used, located beyond the TPC and the TRD (see fig. 5) for a maximum flight length, are a set of RPC (resistive plate chambers) stacks operated with a mixture of $C_2H_2F_4$, isobutane and SF6. The timing accuracy they provide (over a large surface and at modest cost) is about 50 ps when averaging over the 10 layers of a stack of chambers.

The acceptance covers $\eta < 0.9$. Data recorded in a prototype sector exposed to RHIC at BNL[4] shows (fig. 6) the potential of this system, well adapted for momenta below ~1.5 GeV.

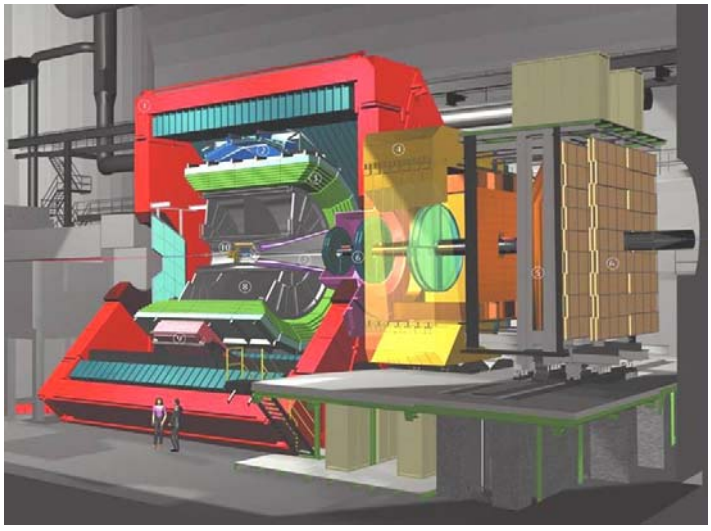

Figure 5: the Alice detector at LHC.

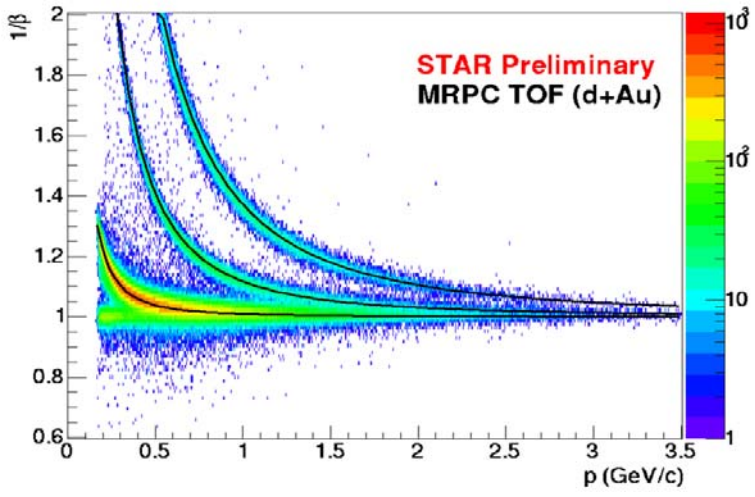

Figure 6: Time of Flight measured at RHIC with an Alice prototype, showing e, π, k, p bands.

2.2 The Alice Time Projection Chamber

At sufficiently low rate (time between events larger than the drift time over the detector length) a TPC is the choice detector for high multiplicity final states.

Several generation of TPCs have demonstrated their potential in these conditions, in particular PEP4 at SLAC, Aleph-Delphi at LEP/CERN, NA49 in fixed target at CERN, STAR at RHIC, ...

Beside pattern recognition and momentum measurement, a recording of dE/dx by ionisation density along the track length gives "some" particle id at low momentum, thanks to its $1/\beta^2$ dependence:

$$dE/dx = k/\beta^2(0.5\ Log(2m_e c^2\beta^2\gamma^2 Tmax/I^2) - \beta^2 - \delta/2) \quad (2)$$

In order to meet the specific constraints from heavy ion collisions, producing mainly particles with low momenta (~150 MeV/c), a light gas is preferable. Alice is going to use Neon instead of the usual Argon based gas. Neon + 10% CO_2 features low electron diffusion, low multiple scattering, and high ion mobility.

The overall size of the Alice TPC is 5m diameter, 5m overall length, giving a record sensitive volume of 88 m^3. A voltage of 100kV on the central plane is necessary to create an electric drift field of 400V/cm, parallel to the magnetic field from the magnet (B = 0.5T). Thanks to the magnetic field the transverse diffusion is suppressed down to $\sigma = 220\ \mu m\ \sqrt{L}(\text{cm})$.

After having drifted along the half TPC length, electrons from ionisation are detected in the end plate chambers equipped with pads of small size (down to 4 mm^2 at inner radius). In total the TPC has half a million electronics channels.

From the above characteristics, Alice expects a dE/dx resolution of 5.5% for isolated tracks and 7% when dN/dy ~8000. Operating at RHIC with a TPC the STAR[4] experiment obtains the performance illustrated in figure 7.

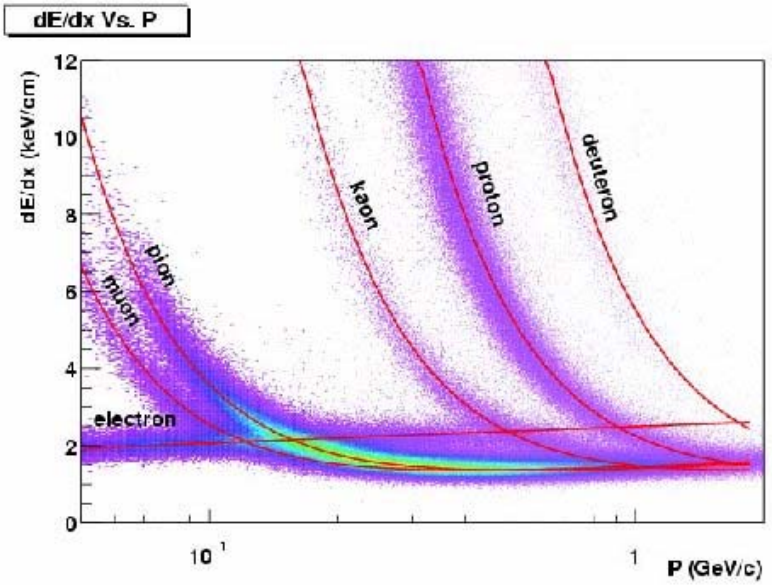

Figure 7: dE/dx in the STAR TPC.

Particle identification in Alice uses several other detectors, also used in other experiments and described later (transition radiation detector, electromagnetic calorimeter, muon filter, ...).

See the Alice Technical Design Report[3] for more details on their specific application to heavy ion collisions.

2.3 CP violation in the b-system with LHCb

The Babar and Belle experiments at the SLAC and KEK-B factories have produced a large amount of data on B^0 and $B^{\pm}$ mesons by running with a large integrated luminosity (several 100 fb^{-1}) at the Y(4S) energy. In particular CP violation in the "golden mode" $B \to \Psi K_S$ was established and measured with a 5% accuracy. Still many cross checks of the Cabibbo-Kobayashi-Maskawa (CKM) mechanism of CP violation in heavy quark decays remain to be done (see fig. 8), both with Bd or Bu as in the B factories, but also in the B_s system, where already the hadronic colliders are contributing (first measurement of Δm_S by CDF at the Tevatron[5]).

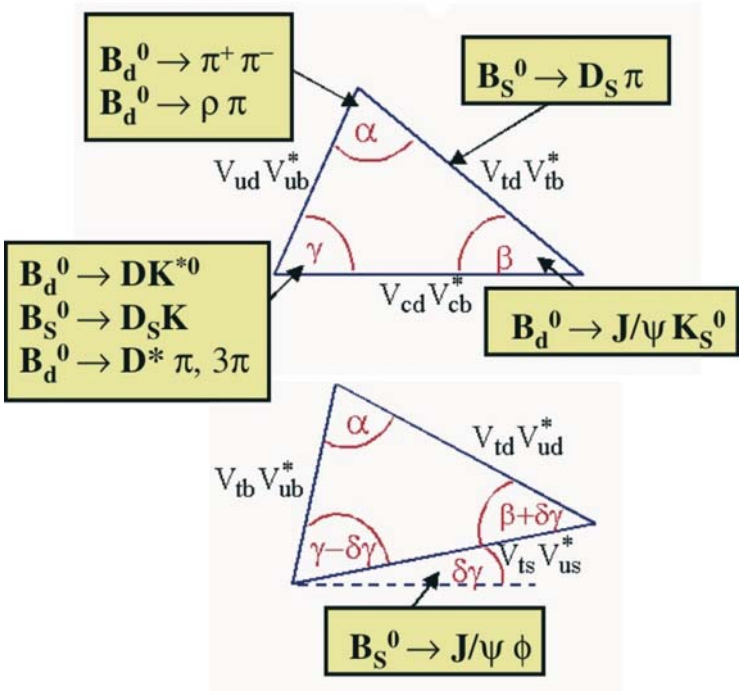

Figure 8: Two unitarity triangles relevant for B physics.

Taking advantage of the large cross-section for B-hadron production at LHC energies (see section 1), and of the lack of forward backward correlation between B-hadrons, the LHCb experiment has chosen to study CP violation in the B system with a single arm spectrometer (see fig. 9)[6].

The acceptance of the experiment is between 10 and 330 mrad meaning a strong boost of all B-hadron decay products. This pseudo-rapidity region is densely populated by minimum bias events, and QCD jet production. In order to avoid difficulties due to pile-up of events for full reconstruction of final states, LHCb chose to concentrate on bunch crossings with one and only one interaction (see section 1).

As is quite obvious from figure 8, many if not all of the interesting final states require π/K/p identification, to be complemented by B or $\bar{B}$ tagging of the companion B. The observation of a visible decay path of the B-hadron is another asset of LHCb, which for this purpose has a highly performing vertex locator.

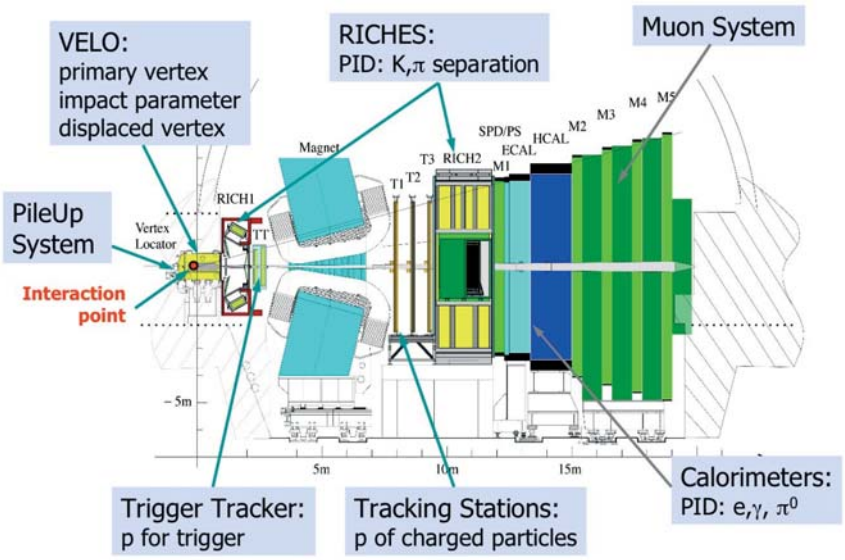

Figure 9: LHCb sketch.

As an illustration for these lectures, some more details are given below the Cerenkov Ring Imaging system (Rich), essential for π/K/p separation. Other detection/identification systems like electromagnetic and hadronic calorimeters,and muon filters present in LHCb are also found in Atlas and CMS where they play a key role and will be thoroughly described.

2.4 The Rich system of LHCb

Given the angle-momentum correlation expected from an "η invariant" production of particles of a limited p_T range ($p_T \leq m_B/2$), the Rich system is divided between two detectors, Rich 1 and Rich 2 covering respectively the large angle-small momentum and the small angle-large momentum part of the acceptance.

Rich1:

Cerenkov photons are produced in two radiators

- The aerogel radiator has a refraction index n=1.03 to which corresponds a maximum angle θ_c (for β=1) of 242mr. With a radiator thickness of 5cm, the expected number of detected photo-electrons (for β=1) is $\sim$7/ring[1].
- The high index gaseous radiator is filled with C_4F_{10} (boiling temperature -1.9°C at normal pressure) with a refractive index n=1.0014 at λ=260nm. The maximum Cerenkov angle is 53mr. With a radiator thickness of 85cm the expected number of photoelectrons per ring is about 30 (for β=1)

Rich2:

The low index gaseous radiator is filled with CF4 with a refractive index n=1.0005 at 260 nm. The associated maximum angle is 32 mr. With a radiator thickness of 180cm the expected number of photoelectrons per ring is about 30.

Given the λ dependence of the radiated photon flux, a maximum sensitivity at short wave lengths is important. Spherical mirrors gather photons emitted in a fixed direction onto a circular image. The mirrors (suitably coated) should be extremely light as they are in the path of particles moving to the downstream part of the detector.

[1] θ_c=Arccos(1/nβ), $dN/dxd\lambda = 2\pi\alpha/\lambda^2(1 - 1/\lambda^2\beta^2)$

The radiator and optical system being defined, the next challenge is the photon detector which should be low noise (to see a single photoelectron), fast (25 ns) and highly granular (given the magnification of the spherical mirror, a granularity of $\leq$ 1 mm in each direction is necessary). To meet these goals a challenging R&D was launched which successfully lead to the HPD (hybrid photon detector). This device has a sensitive photocathode inside an UV transparent window, an internal demagnification of $\sim$5, a large internal gain due to a 20 kV potential between cathode and anode, and a highly segmented anode with 256 x 32 pixels of 62 x 500 μm size. The electronics attached to the pixels is similar to what will be described later for pixel vertex detectors. 500 HPD are necessary for LHCb.

The behaviour of Cerenkov detectors associated to HPD was verified with test beams[7]. A simulation of rings associated to B production in LHCb is shown in Figure 10. It is quite evident from the figure that, beside challenging detectors, particle ID in LHCb will also be demanding in pattern recognition. Another challenging aspect of this experiment is the trigger on hadronic modes of B decays, which starts from an E_T threshold as low as 2 GeV in the hadronic calorimeter (this first step called level 0 -or LVL0- has an expected rate close to 1 MHz).

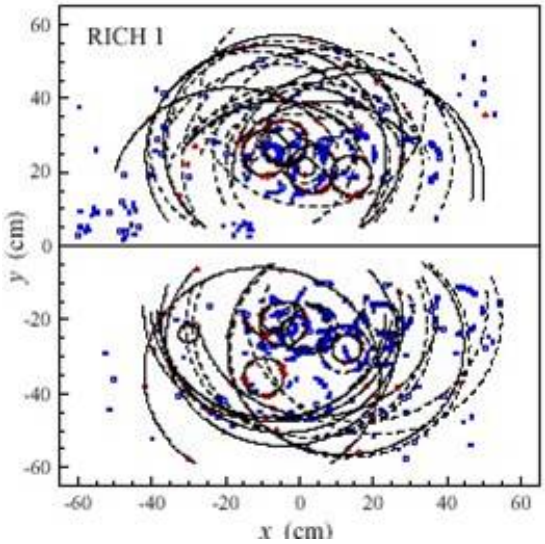

Figure 10: Simulated LHCb rings in a $B\bar{B}$ events.

The reduction of rates goes in several steps:

- LVL1 starting from the calorimeter LVL0 seed walks backward and asks for a track with similar p_T pointing to the cluster, and, in a second step verifies -in 2D and assuming straight tracks- the existence of a detached vertex with a flight distance between 0.15 and 3mm

- LVL2 has now an input rate of $\sim$40 kHz. This allows to reconstruct 3D tracks, make use of the found momentum, and ask for a 3 standard deviation significance of the secondary vertex

- The HLT (High Level Trigger) with an input rate of 5 kHz, has enough computing power to calculate invariant masses, apply particle identification using information from the dedicated detectors -which means finding Cerenkov rings around tracks of known momentum- and select physics channels, in very much the same way as offline software would do.

Most operations being made in a single large PC farm, the distinction between the various trigger levels is more relevant for its logics than from a hardware point of view.

At the end the total rate of writing to tape should not exceed 1 kHz. This rate is ∼5 to 10 times larger than what is planned by Atlas or CMS, but the event size is considerably smaller (factor ∼30).

3 Particle identification in high P_T reactions

3.1 An illustrative example to set the scale

As "pedagogical" example we consider in this subsection, the production of a neutral Higgs boson of mass ∼ 150 GeV, decaying in two Z bosons, one on its mass shell (Z), and one not (Z*). Let's further assume that one of the Z decays in a $b\bar{b}$ pair, and the other in a lepton pair, e^+e^- for example.

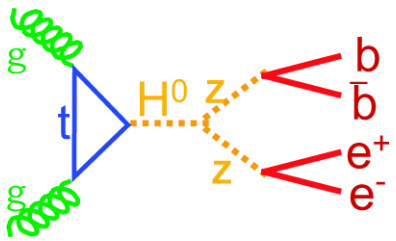

Figure 11: Example of H production graph.

The b quark pair will materialize as two jets (containing each a long lifetime particle). Naively, the final state looks simple: 2 tagged jets from the b quark-partons and 2 electrons. It should thus be fairly clean.

However the QCD coupling constant α_S (Q^2) at the scale of this reaction (Q^2 ∼mH/2) is large enough that, with sizeable probability:

- further gluon lines are attached to initial gluons (or quarks) = (initial state radiation ISR)
- gluon lines are attached to final quarks (FSR final state radiation), not forgetting that some of the debris of the protons may fall into the detector acceptance.

Depending on the random occurrence of ISR/FSR, and on the p_T threshold to define a jet, the "bare" graph above will lead to a final state with 2, 3, 4 jets (plus the electrons). Furthermore, as will be seen later, QCD jets with a small probability can mimic electrons.

The size of the problem appears when comparing the cross-section of the "candidate" reaction gg → H → ZZ → bbee which is expected to be ∼10 fb when branching ratios are included, to the production cross section of events with 4 jets or more, with at least 4 of them with a p_T ∼50 GeV or more which is ∼30 nb: a rejection $\gg 10^6$ is needed. Fortunately an electron appears in general extremely different from a jet. But

- among the backgrounds are $t\bar{t}$ events, $Zb\bar{b}$ events, ... containing also b-jets and electrons with a σ BR of ∼1 pb for the former...
- the situation becomes even more serious when taking "pile-up" into account: at the nominal luminosity of $10^{34}cm^{-2}s^{-1}$, in average 7 x 23 x 5 ∼800 charged, and as many neutral soft particles are produced in any bunch-crossing, in the central acceptance $\Delta\eta$=5, complicating significantly the electron-jet identification.

In order to assess the problem, and the solutions, enlightened by this example, the first step is to understand and describe correctly the way partons hadronize into jets.

3.2 Parton fragmentation

The best studies so far come from e^+e^- annihilations, at the Z^0 pole and below. The main parameters are the transverse momentum of the fragment with respect to the jet axis (parton direction), and the fraction x of longitudinal parton momentum taken by the fragment. The probability to find a fragment "h" with a momentum fraction "x" can be written as:

$$F^h(x,s) = \sum_i \int_x^1 \frac{dz}{z} C_i(s;z,\alpha_s) D_i^h(x/z,s) \tag{3}$$

where D_i^h (x/z,s) is the parton fragmentation function.

At the lowest order in e^+e^- annihilations, Cg=0, Ci=gi(s) δ (1-z).

The evolution of D(x,t) - increase at low x- is reproduced by the Doshkitzer-Gribov-Lipatov-Altarelli-Parisi (DGLAP) equations and was one of the successes of QCD. This effect governs in particular the multiplicity increase of jets with the parton energy (at the Z^0 pole <Nch>$\simeq$20).

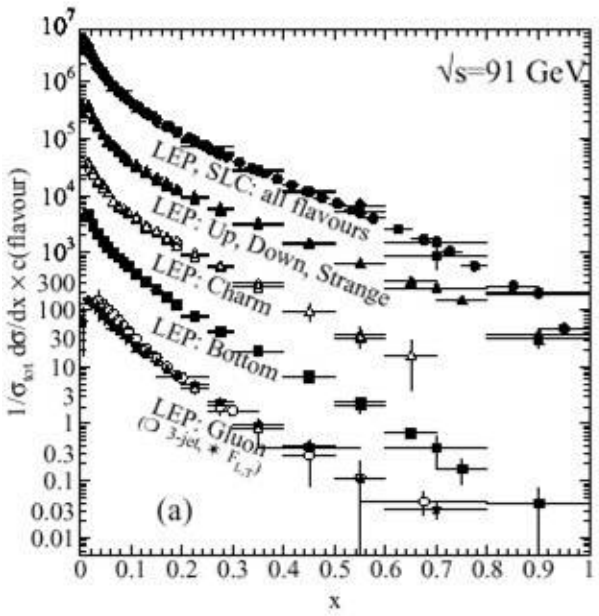

Figure 12: Parton fragmentation.

3.2.1 Heavy quarks and gluons

Flavor tagging allows to separate charm jets and bottom jets from light jets. Furthermore gluon jets can be isolated taking the "third jet" in b$\bar{\text{b}}$g "3 jet" events. Relevant observations are that

- b jets and gluon jets give softer particles than light quarks
- however the fragmentation of a "b parton" in a "b hadron" is very hard (fig. 13).

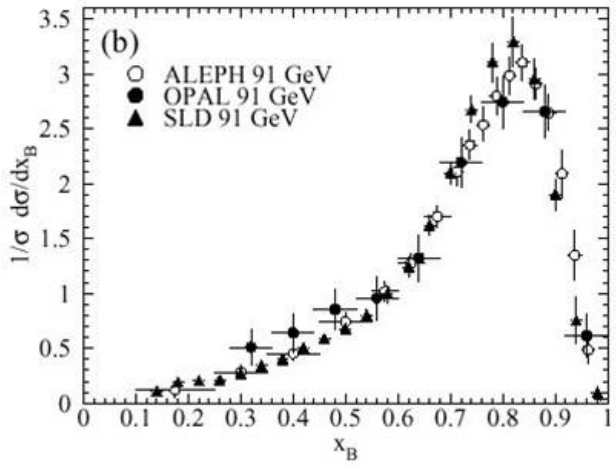

Figure 13: Heavy quark fragmentation to a b-hadron.

3.2.2 Monte-carlo simulation

The string model already developed several years[8] ago allows a rather accurate, although purely phenomenological Monte-Carlo description of the fragmentation process: in short,a string representing the QCD colour field is "stretched" between partons; if the energy stored in the string is sufficient, a $q\bar{q}$ pair is emitted from vacuum, which decreases correspondingly the stored energy. The probability of pair creation is proportionnal to exp-($\pi m_{qT}^2/\kappa$) where

κ = string tension $\sim$ 1 GeV/fm
$m_{qT}^2 = m_q^2 + p_{Tq}^2$
and the z distribution is f(z)=1/z(1-z) exp-(bm_{qT}^2 /z)

The process continues until the stored energy is no longer sufficient to create a new pair. Ad hoc ways are found to conserve the transverse momentum around the string. The creation probability strongly suppresses heavy hadrons -even kaons- in order to reproduce the data (fig. 14).

One of the difficulties in Monte-Carlo simulation of a high p_T final state is to properly bridge the production of partons by QCD showering (perturbative calculations, which can be pushed to Leading Order (LO), Next to Leading Order (NLO), and even NNLO with jet fragmentation, without double-counting. Quite often the parton level calculation is limited to L0, and a scale "k-factor" takes account in an approximate way of higher order effects.

The transverse momentum distribution is assessed by gathering particles in cones of increasing half-angle around the initial parton. Data from Hera and the Tevatron are well reproduced by NLO calculations.

Looking at figures 12 to 14 it can be seen that the probability that a parton fragments to a hadron carrying all its momentum (x=1) is small, but non zero.

When the hadron is a π^0, it may be hard to distinguish the two close-by photons from its decay from a single photon, in which case the jet can be wrongly classified as an isolated photon. If one of the photon converts in an asymmetric way, or if a charged pion falls close to the photon pair induced shower (see below), the jet can be wrongly labeled as isolated electron.

Similarly, fragmentation to a single leading charged pion can mimic the signature of a muon (for example via punch-through, or decay in flight, see below), or even more easily of a τ decaying hadronically.

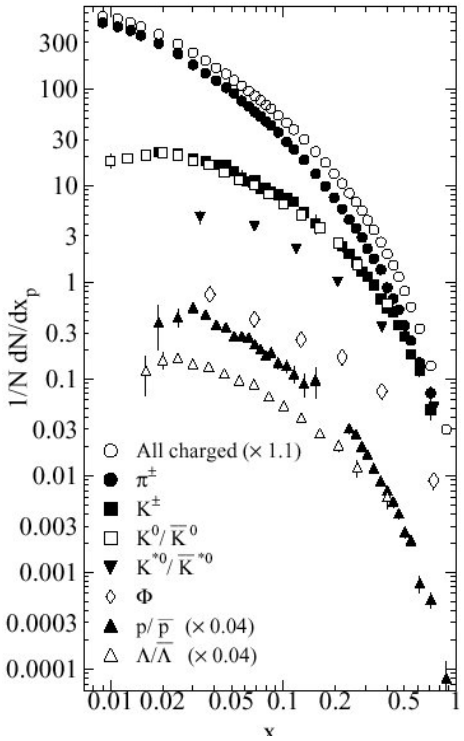

Figure 14: particle species in jets.

3.3 Showering in calorimeters[9]

Charged particles produce curved tracks in the *tracking detectors* placed around the collision point in a magnetic field (solenoidal in general-see below ATLAS and CMS concepts). One can envisage to reconstruct from the tracks the charged component of the jet 3-momentum. However the neutrals (π^0, K^0, n, ...) will be missing, and the sum of momenta of charged tracks can be spoiled by reconstruction inefficiencies. The alternative approach, well proven since now almost 30 years, is to reconstruct the 3-momentum of a jet as the vector sum of energy weighted cells of the *calorimeter* surrounding the tracking detector.

In a high Z, dense material (lead based for example) the first particles to shower are the electromagnetic ones (electrons, photons and thus π^0), because the radiation length X_0 characteristic of the electromagnetic showering process is much smaller than the characteristic length (interaction length Λ) of hadronic collisions affecting charged pions, kaons, protons, neutrons,... During the hadronic cascade, because of strong isospin invariance, π^0 are produced in equal number as π^+ or π^- and thus a hadron-initiated shower develops an electromagnetic component, which can become a fair fraction of the initial hadronic energy when this energy is high enough to generate several steps in the cascade. The reverse is not true: an EM initiated shower remains purely electromagnetic, to 10^{-3} or better. This small component is mostly due to photoproduction of hadrons, a process with a small cross-section.

Muons, like electrons have only electromagnetic interactions. However the related radiation length is much greater than for electrons (by $(m_\mu / m_e)^2$) and thus muons of high energy can traverse several meters of dense material without interaction. This gives a robust way of identifying them as the "only charged particles" remaining downstream of the calorimeter.

3.3.1 Electromagnetic showers

- High energy photon and electron interactions with matter are governed by the radiation length: $X_0(g/cm^2) = 716\ A/Z\ (Z+1)\ \log(287/Z)$ (for lead $X_0 = 6$ mm)

– electrons make bremsstrahlung: after a path-length l the remaining energy of the incident electron is in average $< E > = E_0 \exp(-l/X_0)$. The "missing" energy is carried out by photons, with a spectrum in 1/E

– photons above a few MeV convert into e^+e^- pairs, with a mean free path equal to 9/7 X_0. At energies $\leq$ 1 MeV, photons interact mostly by compton or photoelectric effect (giving a single electron). Around 1 MeV the cross-section of photons is minimum (see fig. 15). As a consequence, photons around 1 MeV have the tendancy to leak out of calorimeters, or absorbers in general.

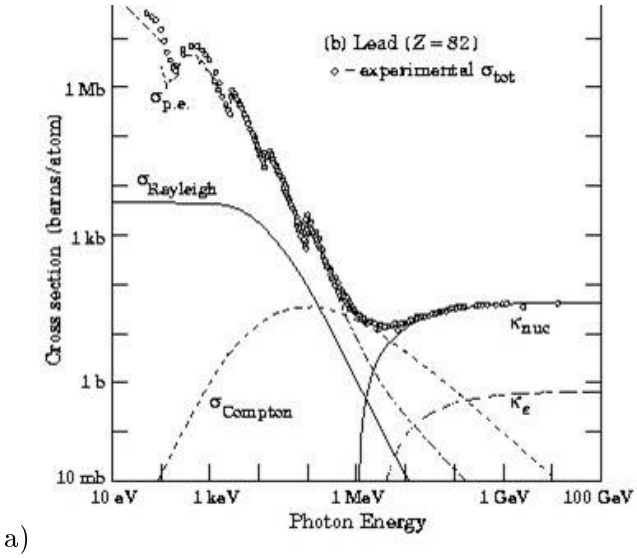

a)

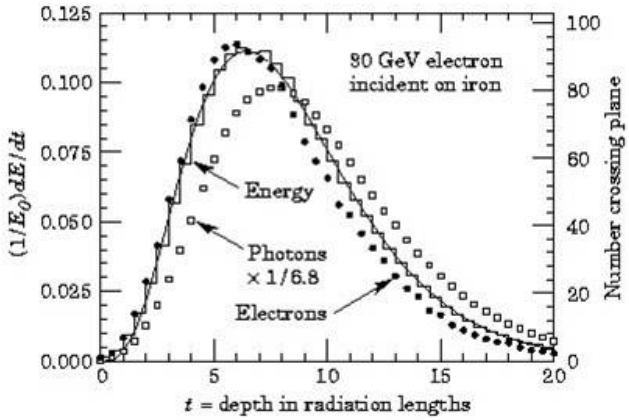

b)

Figure 15: a) : Cross-section of photons in lead. b) Electromagnetic shower profiles.

The combination of the main processes above gives rise to a shower.

- At any energy electrons are subjected, like any other charged particle, to energy loss by ionisation (and Cerenkov if $\frac{v}{c} > \frac{1}{n}$). The energy E_c at which the loss by radiation and by ionization are equal is called the "critical energy" of a material. The process of bremsstrahlung remains dominant until E=E_c. Small values of E_c and X_0 give better sampling calorimeters because there are more electrons and positrons (of lower energy) in the shower. For lead E_c = 7 MeV.

- The longitudinal profile of showers expressed in X_0 is almost material independent, and depends only logarithmically of E. About 30 X_0 (18 cm lead equivalent) are enough to absorb a TeV EM shower (see fig. 15).

- The transverse profile of a shower is driven by multiple scattering (E_s = 21 MeV) of electrons in the shower. It is almost energy independent, and characterized by the Moliere radius $R_M = X_0 E_s/E_c$. R_M is proportional to the material density.
  Accurate and well tested simulation codes (EGS) are available. They have been embedded or transposed in general simulation frames like Geant.

At high enough energy EM shower fluctuations are small, meaning that precision electromagnetic calorimetry is in principle possible.

3.3.2 Hadronic showers

The theory of hadron-nucleus collisions is not able to reproduce data, with multiparticle final states, in a reliable way over a large energy range. To a large extent simulations rely on models interpolating tabulated cross-sections.

The analog of X_0 is the interaction length Λ, mean free path between two inelastic collisions of a hadron. Λ goes with $A^{-1/3}$. In general $\Lambda > X^0$. For iron (lead) Λ = 17cm (18cm), while X_0 = 17,6mm (6mm). Hadronic interactions are more "inelastic" than electromagnetic ones, and 12Λ are enough to absorb a TeV pion. The choice of hadronic calorimeter material is dictated by density, cost, ease of machining, (non) magnetic properties (copper/iron),..

In general a hadronic calorimeter is "non-compensating" with a smaller response for a pion than for an electron or photon of the same energy ($e/\pi > 1$). This is an important limitation which in some cases has been alleviated using (depleted) uranium as an absorber.

From the above, it is easy to understand that Monte-Carlo simulations of hadronic showers are not yet at the level of EM ones. The most accurate codes have been incorporated inside the same frames as mentioned above giving rise to Geant4/LHEP, Geant4/QGSP, FLUKA, ...

3.3.3 Tails in hadronic showers

Hadronic processes have more fluctuations than the electromagnetic ones. As a consequence the probability that some charged particles (pions) remain after a thick hadronic calorimeter, is a slowly decreasing function of its thickness. This phenomenon, known as "punch-trough", complicates the identification of muons: one has to have more absorbing length than strictly necessary for calorimetry (unlike the case of the EM calorimeter), and it is not enough to observe a charged particle downstream the absorber to sign a muon. One has to measure its 3-momentum and bridge it, if possible, to the tracker in front.

4 The ATLAS and CMS concepts-muon detection

4.1 Detector concepts[10]

Both detectors are "general purpose" in the sense that they aim at uncovering any new phenomenon appearing in hight p_T proton-proton collisions, and at measuring expected new particles (Higgs boson(s), SUSY particles, ...) and their interactions as accurately as can be done in the harsh environment of the LHC at high luminosity[10].

ATLAS (figure 16) uses an air toroid to identify and measure muons behind its calorimeter. The central tracking is inside a small 2T solenoid. The calorimeter, in between solenoid

and toroids aims at precision electromagnetic calorimetry with an "accordion" lead-liquid argon calorimeter. Hadronic calorimetry uses copper and tungsten-liquid argon in the forward direction, and iron-scintillating tiles in the central part, less exposed to radiations.

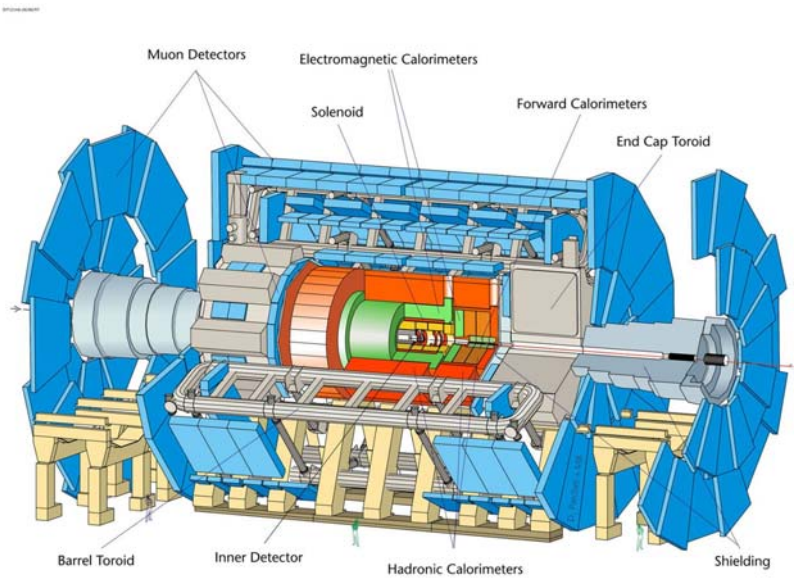

Figure 16: The ATLAS detector.

CMS (figure 17) is a more "compact" detector built around a large and powerful (4T) solenoid. The tracker, the precision electromagnetic calorimeter($PbWO_4$ crystals) and the copper-scintillator hadronic calorimeter are inside the solenoid. Muon identification and detection uses chambers interleaved with the iron flux return of the solenoid.

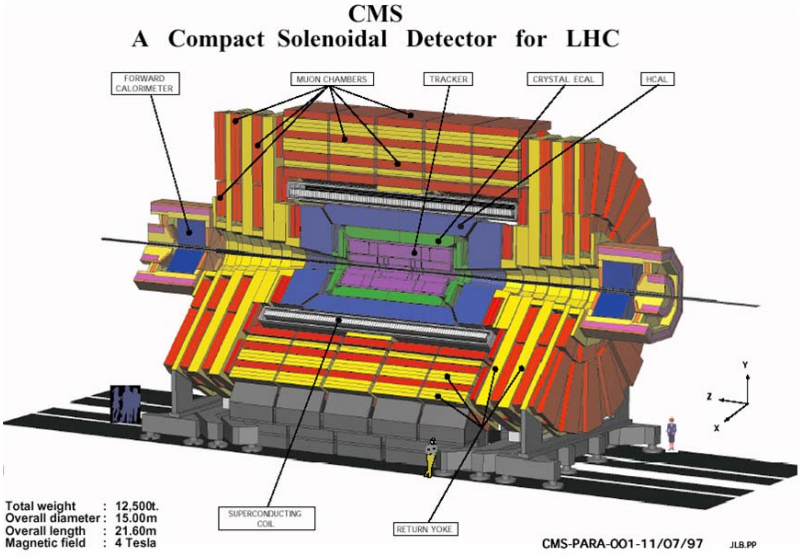

Figure 17: The CMS detector.

4.2 Multi-level pipelined trigger

With a bunch crossing every 25 ns it is out of a question to record events with a simple "interaction trigger" as can be done for example at an e^+e^- machine. The approach used by both experiments is to feed all data from the detectors in a pipe-line of length ∼3 μs (ie ∼120 bunch crossing intervals).

While data progresses untouched along the pipeline, fast processors, using separate dedicated data from some of the detectors (LVL1 data) look for the presence of the searched signatures, namely high p_T electromagnetic showers, muons, and jets. The p_T thresholds for this first step (LVL1) are tuned to leave a "LVL1-accept" rate of at most 100 kHz (ie in average less than one bunch crossing out of 400 is kept).

The ability of the detectors, and fast LVL1 processors, to meet this rejection factor while keeping all (or at least >90%) of the interesting high p_T events is crucial for the experiments.

Beyond LVL1, data are stored on computer farm memories, and more complex algorithms are ran, in an asynchronous way with respect to bunch crossings. The aim of both experiments is to keep interesting events with high efficiency (>90%) while writing to mass storage at a rate not higher than ∼100Hz. The size of the data is estimated ∼1 Mbyte per event.

4.3 Muon detection[11]

4.3.1 Some general features

Starting with Atlas, Figure 18 shows the calculated rate of charged tracks beyond the 12 Λ of the calorimeters and structural iron. The first observation is that punch-through is a small component, meaning all the other tracks are genuine muons, either "prompt", or from π/K decays in the tracker volume (with also a small contribution of decays of particles in the hadronic showers). Among the "prompt" muons, those from b decays dominate at almost all p_T. Muon from charm decays are important at lower p_T, while $W(\rightarrow \mu\nu)$, $Z(\rightarrow \mu\mu)$ become dominant above 30 GeV p_T.

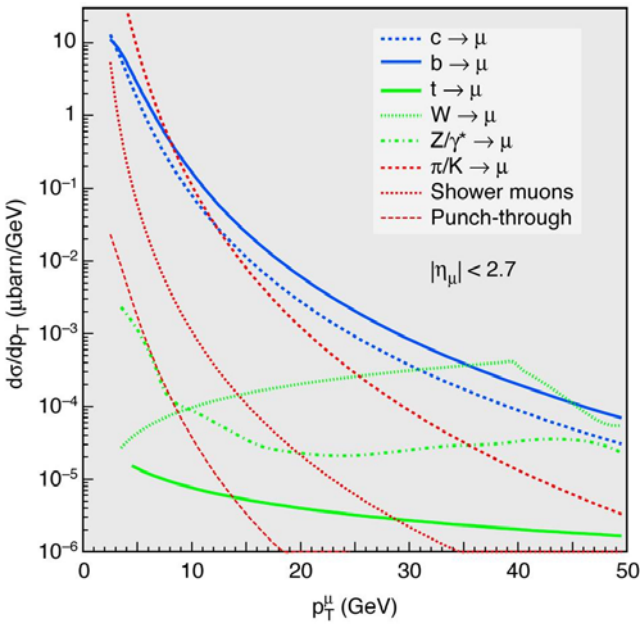

Figure 18: Muon sources in the Atlas spectrometer.

As already mentioned, proton debris from the collision, which carry most of the incident energy, leave the detector in the very forward-backward direction. In order to protect the machine elements (low beta quadrupoles) from the induced radiation, they need to be absorbed locally in a dense shielding. No matter how thick this shielding is (the thicker the better...) neutrons and photons from the very energetic induced showers will leak out and fill the cavern with a kind of "neutron and photon gas". These low energy particles (∼MeV) are however able to interact with the gas of the chambers' spectrometer, producing "single hits". Their rate, strongly increasing with η is calculated to be ∼100Hz/cm^2 for η=2.

4.3.2 Muon triggering in Atlas[12]

The Atlas muon spectrometer consists of three layers of chambers (one before,one inside, one beyond) interleaved with the toroidal magnet system (1 set of 8 barrel coils, each 23 long, and two endcap toroids,each with 8 coils as well, to complete the acceptance down to η=2.7). Each layer of chambers contains a stack of precision drift tubes (except at high η where for rate reasons they are replaced by Cathode strip chambers) dedicated to the measurement of position in the r-z plane with an accuracy of 80 μm).

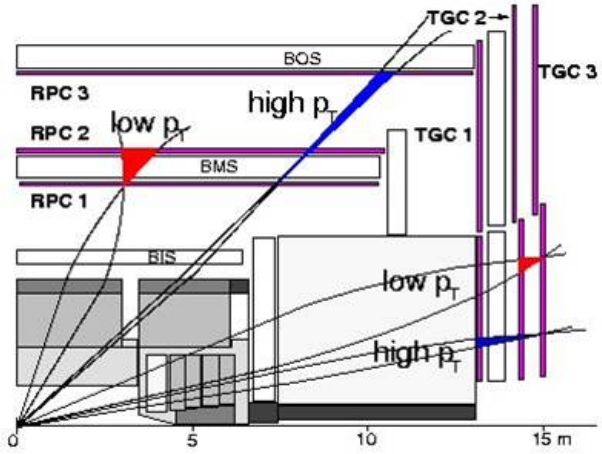

Figure 19: Atlas muon trigger layout.

The central station contains furthermore two sets of trigger chambers with fast response (RPC1, 2 or TGC1, 2 depending on η) dedicated to the LVL1 trigger. The outer station contains one set of trigger chambers (RPC3,TGC3).

The LVL1 trigger logics asks for coincidences between pads in trigger chambers 1, 2 (lower p_T) or 1, 3 (higher p_T). The size and position of the pads are such that the coincidence allows to keep tracks within a certain transverse momentum interval, assuming they come from (or close to) the interaction vertex area.

Starting from the data used to generate Figure 18, plus hypotheses concerning the single hit background, simulations indicate an inclusive LVL1 muon trigger rate of 4 kHz, with a threshold p_T of 20 GeV/c at 10^{34}cm^{-2}s^{-1}. The real physics rates are indeed much lower: for example to the cross-section x branching ratio of a few nb for production of W decaying to $\mu\nu$ in the detector acceptance corresponds a rate of a few 10 evts/s at 10^{34}cm^{-2}s^{-1}.

The higher levels of trigger have the difficult task to reduce the LVL1 rate by rejecting background, without cuting into the physics signal above the LVL1 p_T threshold. For this purpose they should include most of the features of the offline reconstruction (in particular a detailed magnetic field map). Eventually some pre-scaling will be necessary for the lower p_T range.

Conversely, in case one would like to retain more B physics events a lower threshold of 6 GeV/c would induce a rate increase of a factor of 60, only manageable in low luminosity conditions ($10^{33}\mathrm{cm}^{-2}\mathrm{s}^{-1}$ or below).

4.3.3 muon precision reconstruction in Atlas

Several effects limit the precision of reconstruction of muons in a "stand-alone" way in the toroidal spectrometer, the most important being at high momenta the drift tube resolution and the alignment of chamber stacks with each other and with the toroid. On the contrary, at low momenta, the precision is limited by the energy loss fluctuations (dE/dx) in the calorimeter. This limitation can be overcome by successfully bridging muon tracks observed in the spectrometer with their initial part observed in the tracking detector. The expected stand-alone and combined performance are shown in figure 20.

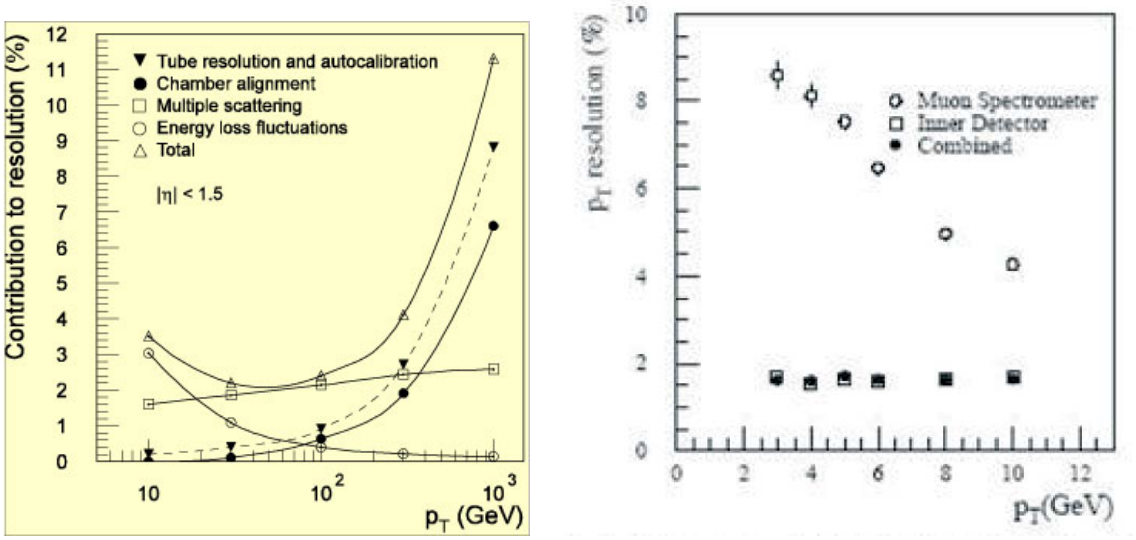

Figure 20: Muon momentum resolution in ATLAS (left: spectrometer alone, right: spectrometer and tracker).

4.3.4 Muon triggering and reconstruction in CMS[13]

As opposed to Atlas, the useful bending direction in CMS is rϕ (ie in the plane perpendicular to the beam direction). The field of the solenoid is much more uniform than the Atlas toroid, and the chamber geometry is simpler (12^{th} fold periodicity in ϕ), resulting in an easier layout for trigger and reconstruction (see figure 21).

Both precision and trigger chambers are "embedded" in the iron flux return of the solenoid after the $\sim 8\Lambda$ of the calorimeter.

As a consequence, punch-through is an important contribution to occupancy in the first layers. Precision drift tubes (rectangular, with electric field compensation) are included in LVL1 for better low momentum rejection.

In a further step, precision points from the drift tubes allow a full reconstruction of the muon track in the flux return, which can then be bridged with track candidates in the tracker sytem in a full 3D reconstruction. Figure 22 illustrates (for L=2 $10^{33}\mathrm{cm}^{-2}\mathrm{s}^{-1}$) the difficulty in making a compromise between acceptable rate at the output of the HLT, and good acceptance for W decays, taken as an example.

As soon as a successful bridging with a track in the central detector is made, the precision obtained by CMS in full reconstruction is better than in Atlas, due to the larger magnetic field

(for η not too large, otherwise the bending power of the solenoid drops out). In a rather wide range of momentum and pseudo-rapidity, it is well approximated by Δp/p=4.5% $\sqrt{p}$(TeV). The muon standalone performance (ie without the tracker, but using the vertex constraint) is about a factor 5 worse.

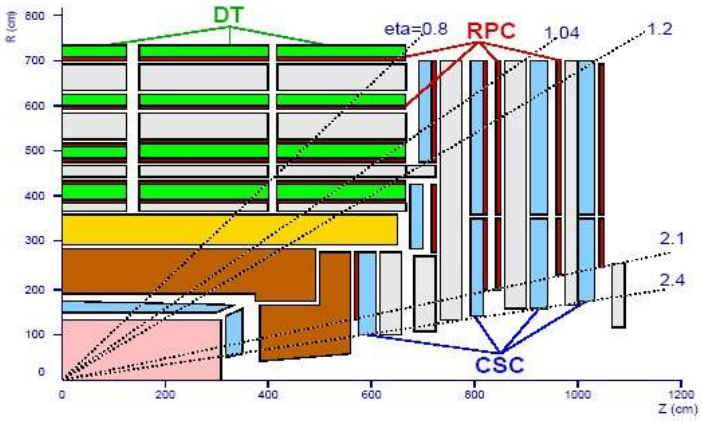

Figure 1: Layout of the CMS muon system.

Figure 21: Sketch of the CMS muon trigger.

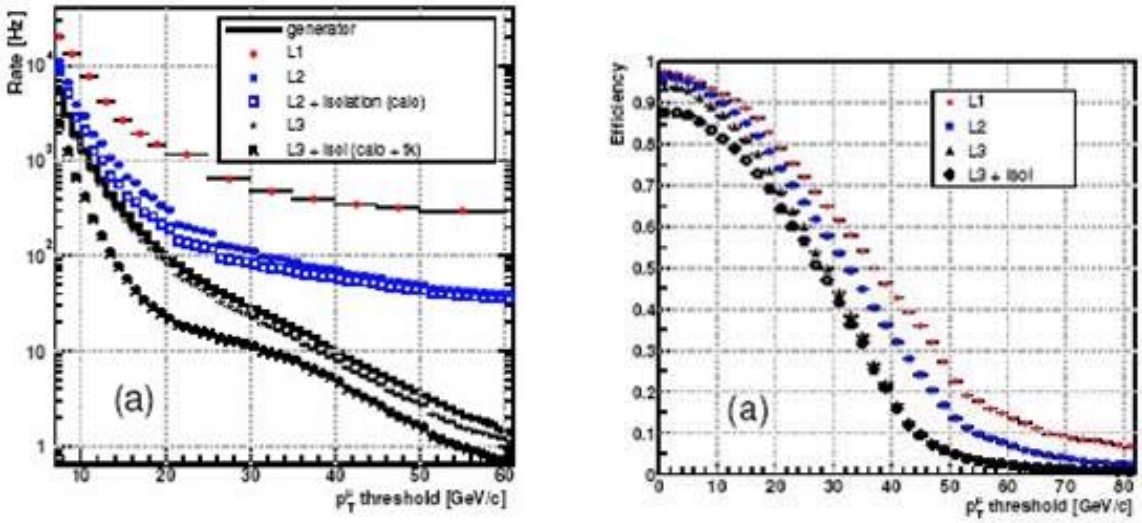

Figure 22: Rate and efficiency for the muon trigger in CMS.

5 Calorimeters and trackers for e, γ, τ identification

5.1 Electromagnetic calorimeter requirements[12, 13]

From the trigger level, to the final reconstruction, the requirements on electromagnetic calorimeters are extremely tight. They have to

- At LVL1 flag EM showers from overwhelming jet "background"
- Provide high level jet-electron and jet-photon rejection

- Provide accurate energy measurement (which requires the calorimeter to be precise, stable, uniform). H $\rightarrow \gamma\gamma$ is the most demanding channel, requiring δM/M=1% or better at 120 GeV
- Be linear over a large dynamic range, from a few MeV (noise) to several TeV
- Provide position measurement allowing, in particular to make a link with the electron track, and to determine, with the vertex, the direction of photons
- Provide accurate timing (100 ps=3cm)
- Provide some angular measurement for photons independent of the vertex point
- Contribute to highly performing jet energy measurement(e/π response)

Not forgetting that the performance should remain stable over several years of running (radiation resistance).

After detailed evaluation and extensive R&D, two different techniques were chosen: "accordion" lead liquid argon in Atlas, and $PbWO_4$ crystals in CMS.

5.2 The CMS crystal calorimeter[14]

$PbW0_4$ was chosen among scintillating crystals because of its good resistance to high radiation levels (when care is taken to eliminate some critical impurities), its fast response (80% of the light is emitted in 25ns) and its compactness (X_0=0.9 cm, R_M=2.2 cm).

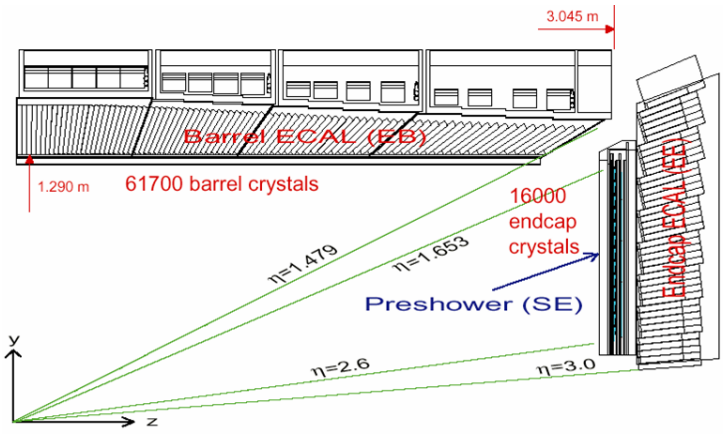

Figure 23: CMS crystal calorimeter layout.

The drawbacks are a low light yield (about 6 photo-electrons/MeV with APD readout) and some sensitivity of the transparency to low levels of irradiation, with fast recovery. This fact will necessitate a continuous follow-up by laser pulses sent to all crystals during "empty bunches" of the LHC cycle.

In order to cope with the situation of the calorimeter in the high magnetic field, avalanche photodiodes (APD) of gain 50 were chosen for the barrel and vacuum phototriodes for the end caps where the level of radiation is higher.

The barrel has 62k crystals of 2.2 $\times$ 2.2 $\times$ 23cm, arranged in 2 $\times$ 18 super modules, and the end-caps 16k crystals of 3 $\times$ 3 $\times$ 22cm, arranged in two Dees per side. The front-end electronics

features a preamplifier and shaper in CMOS-250mm technology with 3 gains, followed by one 12-bit adc per gain. The noise is about 30 MeV per crystal.

Calibration strategy:

From bench test at production the response dispersion of crystals + APD is about 4% rms. It was recently shown that the use of cosmic muons during tests before modules insertion in the coil can improve this knowledge down to 2% rms.

The modules which were exposed to beam (25%), will be used to verify that final calibration with electrons from W decays (E/p) and Z decays using the Z^0 mass constraint give a calibration good to 0.5% rms. Such a procedure shall require several months of LHC collisions at $10^{33}cm^{-2}s^{-1}$ for crystal by crystal calibration. The laser monitoring will be used to absorb short-term variations due to irradiation.

Shower reconstruction:

In the absence of magnetic field,the energy of the initial electron is estimated from a 3 × 3 or a 5 × 5 cluster.

The energy resolution obtained in test beam, locally[14], is well fitted by

$$\left(\frac{\sigma}{E}\right)^2=\left(\frac{2.9\%}{\sqrt{E}}\right)^2+\left(\frac{125(MeV)}{E}\right)^2+(0.30\%)^2 \quad (4)$$

The position resolution from a barycenter is better than 1mm at 30 GeV.

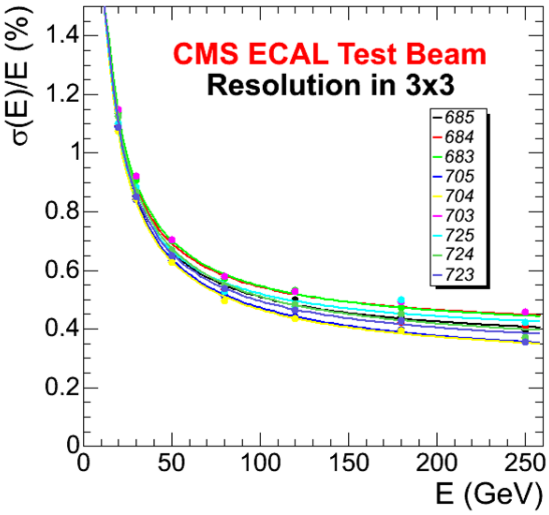

Figure 24: Crystal calorimeter resolution in test beam.

5.3 The ATLAS accordion calorimeter[15]

From previous experience, a lead-liquid argon sampling calorimeter is known to be stable, and intrinsically uniform. The accordion shape (figure 25) brought in the possibility to get a fast response when coupled to suitable electronics shaping, and to implement high granularity without cracks. Built from 1.2mm lead foils (1.5mm for $\eta > 0.8$ and 1.7mm for $\eta > 1.4$) glued in between thin (0.2mm) stainless steel sheets and spaced by 2×2mm gaps around the 3-layer readout electrodes (variable gaps for $\eta > 1.4$ in the end-caps) the Atlas calorimeter is less dense than the crystals of CMS ($X_0 \sim 2$cm and $R_M \sim 4$cm).

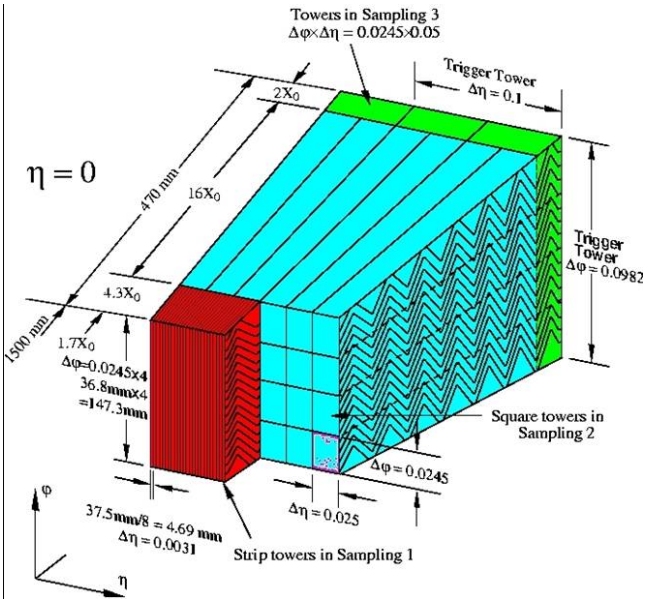

Figure 25: Sketch of the "accordion" geometry..

The calorimeter features 3 samplings in depth: front with $\Delta\eta \times \Delta\phi = 0.008 \times .1$, middle with $\Delta\eta \times \Delta\phi = .025 \times .025$, and back with $\Delta\eta \times \Delta\phi = .050 \times .025$. The calorimeter itself is preceded, in the same cryostat, by a presampler with granularity $.025 \times .1$, whose main role is to correct for energy lost in the upstream material. The inner radius of the barrel calorimeter is 1.5m and its total length 6.5m. The magnetic field at the location of the calorimeter is few tens of mT. The calorimeter is built out of 2 x 16 modules. Thanks to the accordion geometry, the calorimeter is fully uniform in azimuth after assembly.

Showers are reconstructed in clusters of 3×3 cells in the middle compartment, with the corresponding coverage in the presampler, front and back compartments. Such clusters contain 93% of the energy deposited by a high energy electron or photon. The sampling term of the energy resolution is $10\%/\sqrt{E}$ and the noise in a middle cell 30 MeV (ie ∼200 MeV for a cluster). The electronics chain starts with a current preamplifier, followed by a 3 gains shaper and analog sums for the LVL1 primitives. Data are stored in an analog pipeline before being digitized (12 bit adc) upon LVL1 trigger request. In total there are 180 thousand electronics channels.

In a liquid argon calorimeter the cell to cell calibration is purely electronic. In Atlas this system was designed with particular care, with an uniformity of 0.25%, as demonstrated in test beam, where using the electronics calibration alone a global uniformity of 0.6% per module was demonstrated[16]. In the energy region 15 to 180 GeV, critical for several precision measurements (W mass, Higgs mass, ...) the linearity of the calorimeter was shown to be better than $\pm$ 0.1%[17]. Between $m_W/2$ and $M_Z/2$ it is $\sim 2.10^{-4}$ a value needed to measure the W mass with a 15 MeV accuracy (see figure 26).

The absolute "mass scale" of the calorimeter will be established using the Z mass constraint. Because of the effect of the inner tracker and solenoid material present in Atlas (see below) and not in test beam, it was estimated that one can assume uniform response in sectors of 0.2×0.4 and readjust any longer ranger variation with the Z mass constraint. This leaves 448 sectors to be readjusted, for which a few days of data at $10^{33}\mathrm{cm}^{-2}\mathrm{s}^{-1}$ (few 100 k events) should be enough.

The granularity of the calorimeter allows accurate position measurements, and shower direction measurement (thanks to the 3 samplings) with an accuracy of $50\mathrm{mr}/\sqrt{E}$.

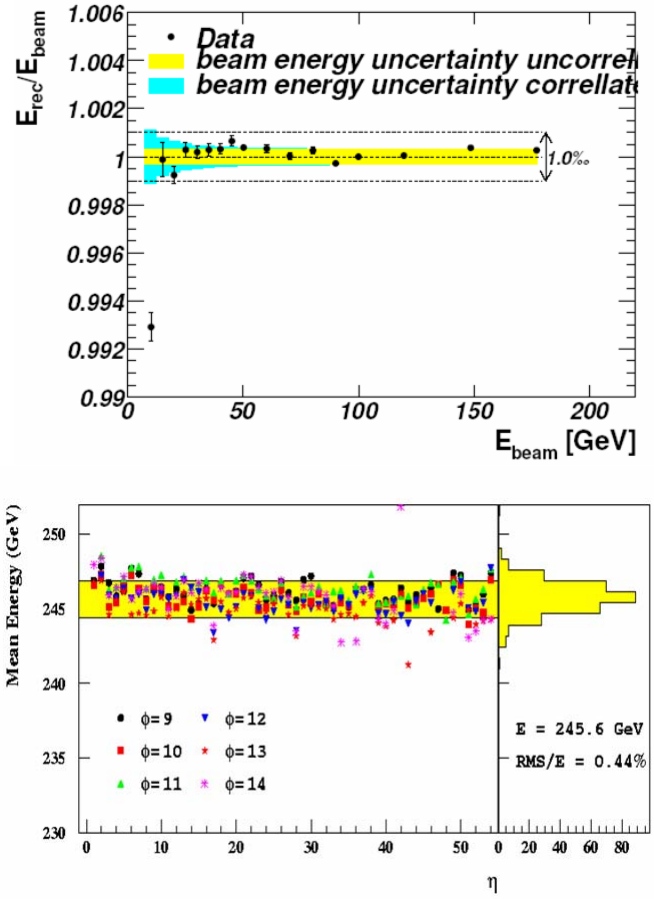

Figure 26: a) Atlas EM calorimeter linearity. b) Atlas EM calorimeter uniformity.

5.4 Electromagnetic shower identification at LVL1[12, 13]

The basic approach is to "digitize and sum" (CMS) or "sum and digitize" (ATLAS) signals from a "small" $\Delta\eta \times \Delta\phi$ region -but large enough to fully contain an EM shower, (actually 0.1×0.1 in Atlas, ie 4×4 middle cells and $.087 \times .087$ in CMS, ie 5×5 crystals)- and compare the sum to a given threshold.

In practice 4 sums of 2×1 such "trigger towers" are built to get rid of edge effects,and compared to an E_T threshold (see figure 27). The surrounding cells in the EM calorimeter, and the "image" area in the downstream hadronic calorimeter are compared to a low E_T threshold if one is to require isolation.

An Asic implemented logics treats in parallel all 0.1×0.1 trigger towers (3200 such towers cover the trigger space $\Delta\eta \times \Delta\phi = 5\times6.28$) realizing the equivalent of a "sliding window" over the whole calorimeter,... in 25 ns.

The background from QCD jets is huge, but decreases fast with E_T (Fig. 28). Taking into account that jets are broad,asking for "isolation" lowers the rate, but pile-up may kill good candidates.

An estimation of the rate expected in CMS at $10^{33}\mathrm{cm}^{-2}\mathrm{s}^{-1}$ is shown in figure 28. It is entirely dominated by QCD jets. The rate expected with a 20 GeV E_T threshold (6 kHz without isolation) should be manageable at 10^{33}, but will saturate the bandwith at 10^{34}, thus requiring a higher threshold or some downscaling. The rates expected in Atlas are similar (albeit somewhat higher).

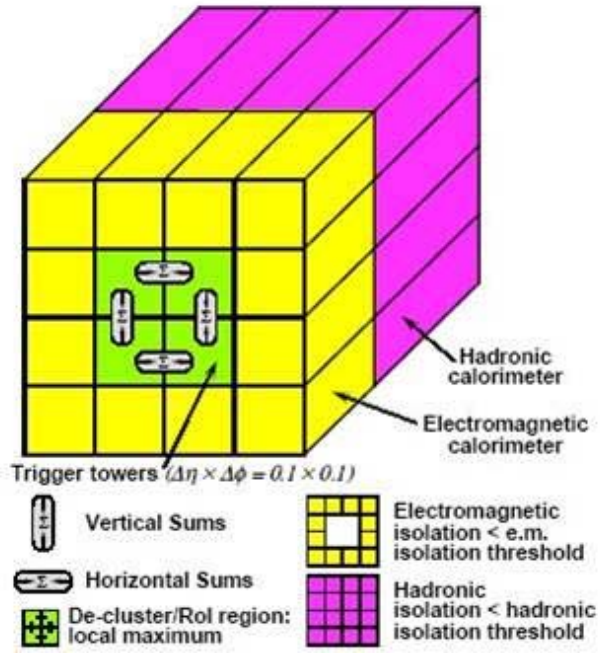

Figure 27: EM calorimeter LVL1 trigger sketch (ATLAS).

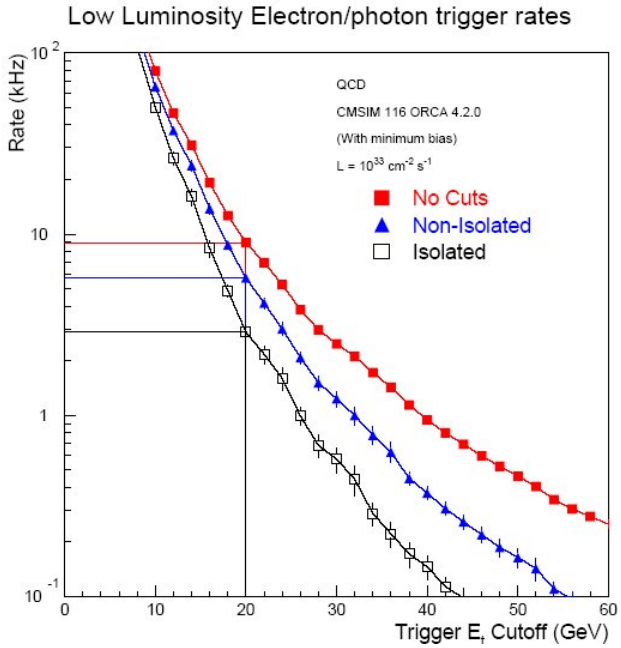

Figure 28: CMS EM shower LVL1 rate.

In order to reduce, in the subsequent trigger levels, the QCD background rate to what is compatible with the experiments DAQ (∼100 Hz in total), information from the tracking system is necessary. The basic approach is to require either:

i) a track pointing to the cluster candidate (with a ratio energy/momentum compatible with 1) for an electron candidate, or

ii) "nothing" in front of the cluster for a photon candidate. Actually because of the non

negligible material of the tracker itself, e^+e^- pairs resulting from conversion need also to be allowed.

5.5 Atlas and CMS tracking systems[18]

The CMS tracker is a full Silicon system, 5.4m long and 2.4m in diameter, made of a set of cylinders in the barrel part and forward disks (see figure 29). In total the system counts 25000 Silicon sensors (figure 30) for a total area of 210m^2, an order of magnitude more than was built so far. The readout is organized in strips of ∼10cm length and a pitch between 60 and 120 μm. Some of the sensors have a double-sided readout. In total there are 10 millions strips, each readout by a charge preamplifier-shaper (50ns time constant) realized in 250 nm CMOS technology, followed by an analog optical transmitter and a 10-bit flash ADC outside of the tracker volume.

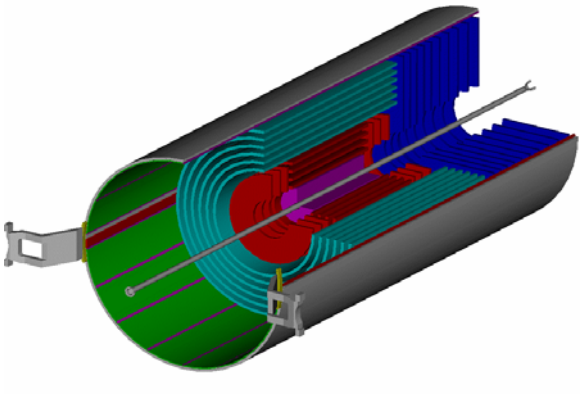

Figure 29: The CMS tracker sketch.

Figure 30: A barrel Si strip module of CMS.

The analog readout was chosen for easier control, and possibly better position resolution from interpolation between strips.

One of the major difficulties was to design sensors and electronics maintaining their performance under irradiation. The radiation flux is of course larger at small radii, with an anticipated figure at 20cm radius of 1.6×10^{14} 1MeV n-equivalent/cm^2 for 5 years at high luminosity. In order to reduce the effect of radiation damage to the sensors (charge trapping centers) the full volume (24m^3) will be kept at -10°C during all the life of the experiment -except short maintenance periods.

Close to the beam pipe, where the radiation flux is even higher, a 3 cylinders + disks pixel (size 100 × 150 μm) system of 67 million channels completes the tracker system.

The sensors themselves, the front-end electronics, the cooling pipes, the mechanical supports, the power and readout cables,... unavoidably generate a non-negligible amount of material through which electrons and photons will start to radiate/convert.

The simulated energy spectrum of a 35 GeV electron E_T in the barrel, even reconstructed with a "hybrid super cluster algorithm for LVL2", shows (figure 31) a characteristic low energy tail due to bremsstrahlung photons escaping the cluster. In this respect the high value of the CMS field (4 Teslas) is a penalty.

Starting from the inside, the Atlas tracker system is composed of a 3 cylinders and disks pixel system (see section 7 for more details), surrounded by a silicon strip detector (SCT) up to a radius of 52cm. Between the SCT and the warm inner cylinder of the liquid argon calorimeter housing the solenoid (R=1.24m) is located the transition radiation tracker (TRT) which covers radii between 56cm and 108cm, and goes longitudinally up to z=±3.4m.

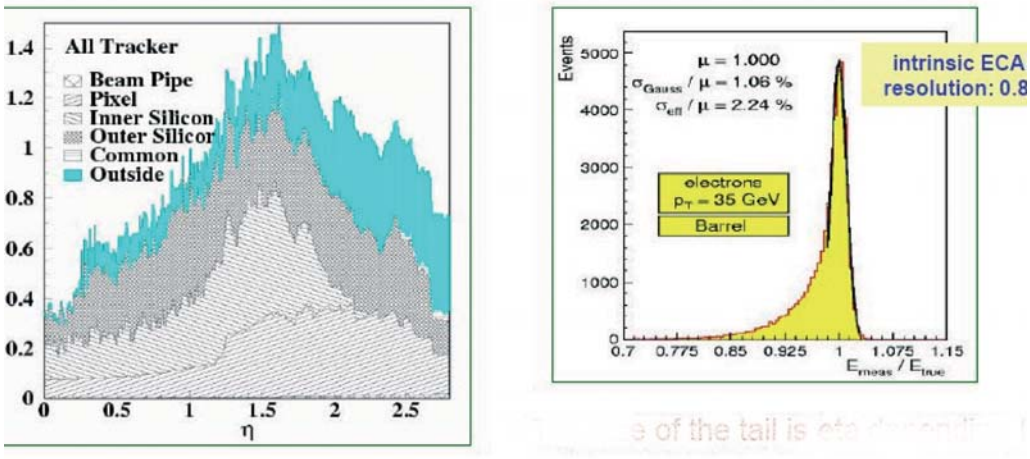

Figure 31: The CMS tracker material (in X_0) and the energy spectrum of a 35 GeV P_T electron.

As compared to CMS, the SCT system of Atlas has "only" 60m^2 of active silicon area, uses single-sided sensors of the "n-on-n" type with a pitch of the readout strips of 80 μm. The front-end electronics features a 25ns shaping time constant, and a discriminator providing for each channel,every 25 ns a "0" or a "1" stored in an on-detector digital pipeline readout under LVL1 request. The expected signal/noise ratio is about 15 (11) for un-irradiated (exposed to 10^{14} p/cm^2) detectors. The SCT has 6.6 millions of channels.

The Transition Radiation Tracker consists of a stack of straw tubes filled with a Xenon rich gas mixture, alternating with thin foils of light material (CH_2). When a relativistic charged particle crosses a large number of thin foils (CH_2)/vacuum transitions, it emits photons in the X range if its Lorentz factor γ is large. The integrated intensity of the emitted radiation is proportional to γ, while the number of photons above a given threshold increases like log2γ. Emitted X-rays materialize in the Xenon rich gas of the straw tubes (4mm in diameter) giving large signals ($>\sim$6 keV against $\sim$2 keV for dE/dx).

The Atlas TRT is divided in a barrel part with straws of 2×70cm length, and a set of wheels. A straight track from the vertex crosses typically 35 straws. Given the comparatively large area of a straw compared to a Si strip their occupancy is high, particularly at high luminosity (between 10% and 40% depending on the location of the straw), but given their high density along a track they remain a powerful pattern recognition tool, together with giving good precision on the sagitta (momentum) measurement. The functionalities briefly described above require electronics with two charge thresholds, and an associated time measurement with a TDC to reach a precision of $\sim$170 μm per straw. In total the TRT has close to 400 thousand channels.

In clean conditions (beam test) the TRT detector itself provides an electron/pion separation particularly effective at relatively low energy (20 GeV and below). As an illustration, for a 90% electron efficiency, the rejection of pions at 20 GeV is between 15 and 100, depending on η through the number of crossed straws.

5.6 Electron and photon ID at LVL2 and beyond[12, 13]

5.6.1 electrons in Atlas

The first step is to refine the calorimeter conditions, using the full granularity available at LVL2, together with a more refined calibration as compared to LVL1.

Taking Atlas as an example, figure 32 illustrates the rejection power of a cut on R_{37} the ratio of the energy in a 3×7 cluster as compared to a 7×7 cluster.

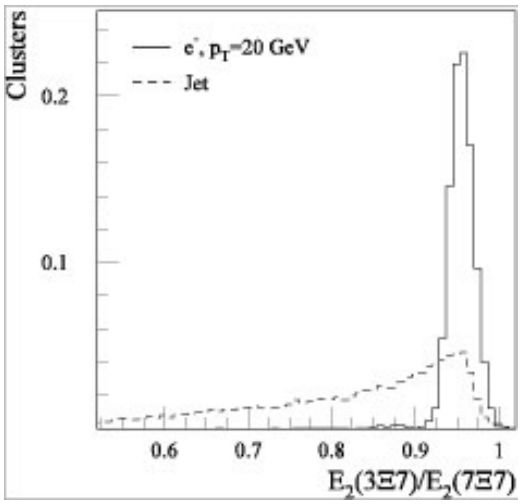

Figure 32: Shower shape at LVL2 in Atlas.

The next step for an electron trigger is to require a track in the ID (using the calorimeter cluster as a seed) in a 0.1 × 0.1 window, and then to ask for a matching between the track and the cluster, both in position and energy/momentum ratio.

Starting from a LVL1 rate of 12 kHz at 2×10^{33} for a threshold of 25 GeV E_T, the simulated rate decreases to 2 kHz after the refined calorimeter cuts, and to 500Hz after the track matching (incl E/p).The final reconstruction, which to a large extent can be implemented in the "event filter" as the last step of the online selection (so called HLT) brings the rate down to 30 Hz, with an overall efficiency of ∼80%. The rate of prompt electrons with this threshold is about 10Hz.

5.6.2 electrons in CMS

The selection process is similar in CMS, with the difference that after having found a cluster passing all electromagnetic cuts in the crystal calorimeter, one looks for pixel hits at the place where an electron track of either sign would have passed. In case of success tracking proceeds from these seeds, gathering strips from the silicon strip detector. The efficiencies for signal and background obtained by simulation of the complete LVL1+HLT process are grouped in the table below, for a luminosity of 10^{34} and a threshold of 30 GeV E_T.

Signal	**Background**
W → eν =35 Hz	Charged/neut π overlap = 15Hz
	π^0 Dalitz and conversions = 19Hz
	b/c → e+X = 6Hz
Total = 35Hz	Total = 40 Hz

The total calculated rate is very close to the maximum allowed.

5.6.3 photons in Atlas

The same "shower shape" criteria as for electrons are applied, at LVL1 and in the first step of LVL2. Then the selection follows two branches in parallel:

- *Converted photons* (with R_{conv} <∼60cm-30% of cases) resemble more electrons. One or two tracks are found pointing to the cluster, and the track match and E/p tests are possible, although being more complicated when there are 2 tracks

- *Unconverted photons* (∼70% of cases) a track veto is applied, then a specific rejection against isolated π^0 s is made, exploiting the fine granularity of the first sampling of the calorimeter ($\Delta\eta$ = .003 or 5mm). To set the scale,the two photons of a 60 GeV E_T symmetric π^0 decay are separated by >7mm at the calorimeter front face. Detailed simulations and test beam studies have shown that an extra rejection factor of ∼3 can be gained[19].

These rejections can be combined with track isolation in the tracker, keeping the efficiency for photons in a given process fixed.

Overall, in photon jet-events at high p_T ($\geq$ 50 GeV/c), a rejection of 1050 against quark jets is found, which increases to a factor 6000 against gluon jets, due to their softer hadronisation (see section 3.2).

At the trigger level it is estimated that at high luminosity a threshold as high as 60 GeV E_T is necessary to keep the rate of single photon trigger below the electron rate (for 20 GeV E_T). Indeed a coincidence of two photons with thresholds of 40 GeV and 20 GeV can be used in order to gather candidates for the H→ $\gamma\gamma$ mode (see below).

5.6.4 photons in CMS

Selection of photons in CMS uses similar criteria, starting with shower shape cuts in ECAL (in η only, due to the strong effect of the magnetic field on converted photons). Further rejection is obtained by applying isolation in an ECAL ring (<4 GeV in .06 <<.35) and an energy leakage cut in HCAL (<8 GeV in ΔR=0.4). Finally a track isolation cut (no track of p_T>1.5 GeV- except matched conversion- in ΔR=0.3) is applied. An illustrative performance is that γ+jets events with kinematics similar to prompt $\gamma\gamma$ events with $M_{\gamma\gamma}$ ∼120 GeV are rejected by a factor about 100. The rejection performance at this stage is inferior to what is expected from Atlas .

6 Jets, Missing E_T, τs, Ws and Zs

6.1 Jets[20]

Jets are comparatively easier to trigger on and reconstruct. Since the production cross-section decreases very fast with E_T, an accurate E_T measurement at the trigger level is important. In this respect collecting energy in a large cluster, like 0.8 × 0.8 or more, as well as weighting correctly the EM and HCAL energies (ATLAS and CMS calorimeters are non-compensating...) are important. On the other hand it is also important to separate nearby jets, which calls for smaller cluster sizes.

ATLAS works with a 4×4 window of 0.2×0.2 trigger cells. A LVL1 internal logic eliminates double counting and finds the core tower of a triggering jet, which in turn defines a "region of interest"-or RoI- for subsequent processing in HLT. Like for the EM trigger the logics is equivalent to sliding a window over the whole calorimeter, every 25 ns.

Monte Carlo simulations, backed by test beam results,show that the jet energy resolution,after careful offline calibration is well reproduced by σ(E)/E=a/$\sqrt{(}E)\oplus$b/E$\oplus$c the sampling term (a) being about $0.7\sqrt{(}GeV)$ for Atlas,somewhat larger in CMS due to the coarser sampling and limited depth of the hadronic calorimeter, and the spread of charged tracks induced by the strong magnetic field. The noise is a few GeV, and the constant term, dominant for high energies, ranges from ∼3% to ∼10% depending on the η range and the experiment.

6.2 Missing E_T at the trigger and reconstruction level

From the position and energy of each of the calorimeter cells, are calculated, summing on the EM and HCAL sections with the proper weights:

- $\sum E_x$ and $\sum E_y$ a 2-vector in the transverse plane whose modulus is $E_T$miss
- $\sum E_T$ in the transverse plane, also called "total E_T"

If there are no missing particles $\sum E_x = 0$ and $\sum E_y = 0$, the accuracy being of course limited by several effects, in particular

- the fluctuations of the sampled energies
- the noise in each calorimeter cell (an option is to include in the sum only those cells with an energy above a threshold, for example, two times the noise).
- the un-instrumented part of the solid angle (η >5) where the energies are high, but the associated E_T rather small due to the sin(θ) factor
- cracks,...

Conversely E_T miss > E_{th} signs (a) missing particle(s): a neutrino(s) or something more exotic...

Detailed Monte-Carlo simulation of different types of events have shown that the resolution in $E_T$miss is rather well described by $\sigma(E_T \text{ miss}) = K/\sqrt{(\sum E_T)}$, with K ~0.5 $\sqrt{(GeV)}$ in Atlas, somewhat larger in CMS for the same reasons as for the jet resolution.

An example of what can be achieved with $E_T$miss is shown in figure 33, from CDF, in which is plotted the reconstructed value of this variable for events with an isolated electron of p_T >25 GeV/c. This sample is dominated by W decays, and the plot shows,well separated from each other, the remaining QCD contribution and the signal corresponding to the escaping neutrino from Ws.

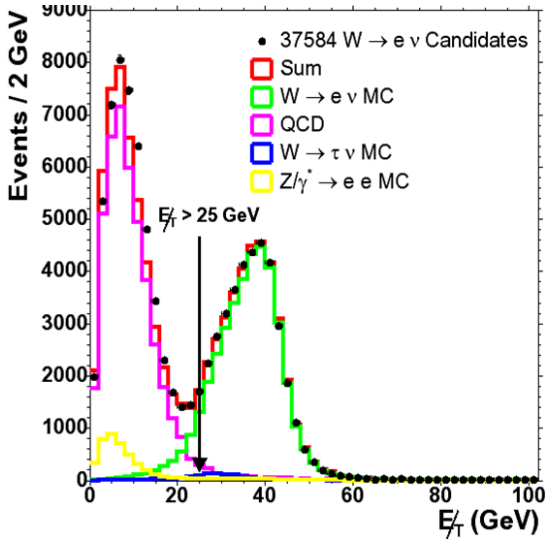

Figure 33: E_T miss in CDF for events with isolated high p_T electrons.

At the trigger level $E_T$miss cannot be used in standalone because of the above mentioned effects affecting its resolution,and particularly because of tails in the energy resolution of jets. Instead this signal will be combined with other trigger signals, in particular those able to sign a τ.

6.3 The third lepton: τ identification

Beside being a third lepton with the same coupling to W and Z as the electron and the muon (EW universality), the τ, because of its much higher mass (1777 MeV against 0.511 and 105 respectively) has a much higher potential for standard model Higgs physics (coupling constant proportional to the mass) and super symmetric Higgs. The leptonic decay modes of the τ (17% $e\nu\bar{\nu}$, 17% $\mu\nu\bar{\nu}$) are selected through the decay lepton, however with a reduced efficiency due to the tranverse momentum lost in favour of the neutrinos.

The hadronic decay modes appear as a single track (11% $\pi\nu$, 38% $\pi\nu$ + neutrals) associated to a shower extending in the hadronic calorimeter, and for a small fraction (9% $3\pi\nu$, 5% $3\pi\nu$ + neutrals) as a very narrow jet of 3 particles, with an associated shower extending into the hadronic calorimeter as well.

τ-jet identification at the trigger level in Atlas

The criteria used at LVL1 for the calorimeter part are similar to those used for EM showers selection, with the difference that the energy in the 2×1 cluster now includes the hadronic part. At LVL2 the ratio R_{37} with a threshold value of 0.9 is quite effective: at 2×10^{33} those criteria together, with a threshold of 35 GeV E_T, reduce QCD jets to a manageable rate of 2.3 kHz with a 60% acceptance for τ jets.

In order to cope with the DAQ limitations, further conditions are added in LVL2 and HLT, in particular including a missing transverse energy condition (see above), or the request of two τ_s in the event.

6.4 Offline τ identification and reconstruction in Atlas[21]

When a single particle is missing, E_T miss as described in 6.2 is the estimate of its transverse momentum. If two non collinear particles are missing the measurement is ambiguous. This ambiguity can be resolved when the mass of the two parent decaying particles are small as compared to the other transverse momenta in the event. This for example is the case for events containing a $Z \to \tau\tau$ or an $A \to \tau\tau$ decay.

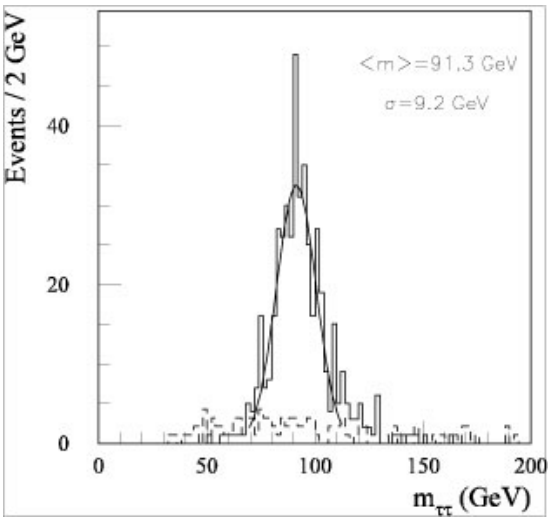

Figure 34: Reconstructed $Z \to \tau\tau$ mass in Atlas.

In this case one can assume that each of the p_T of the two missing ν_s is collinear with the other (observed) decay products of each mother particle, and reconstruct the transverse

momenta of each neutrino by projecting E_T miss on these two directions (which should not be collinear).

Despite the reconstruction trick briefly described above, events with 2 τ_s, both decaying hadronically, may not be easy to unearth from QCD background.

A detailed simulation made recently in Atlas shows however that this should be possible with a reasonable efficiency (∼50%) by using all discriminating variables available from the detector (see figure 35). These includes:

- the number of charged tracks (1,or 3 not all of the same sign)
- R_{EM} the radius of the shower in the EM calorimeter (fig. 35a)
- E_{T1-2} the transverse energy between 2 rings around the shower center (fig. 35b)
- $\Delta\eta$ the width of the energy cluster in the front compartment (strips) (fig. 35c)
- E(calo)/p(tracker) for 1 and 3 track events (fig. 35d)
- the impact parameter of the tracks (fig. 35e)

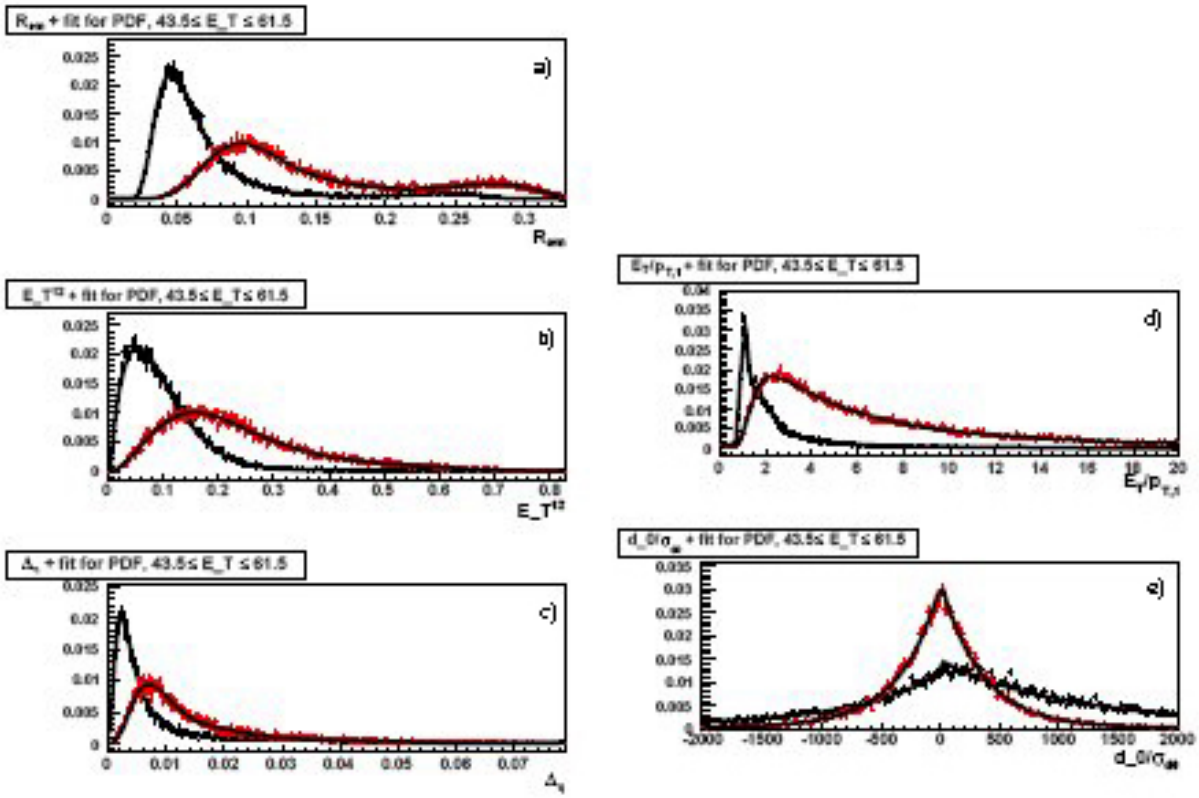

Figure 35: τ identification variables in Atlas (black: τ, red: QCD jets).

For a 50 GeV E_T τ-jet transverse energy, the rejection against QCD jets is about 1000, for a τ acceptance of 50%, a figure good enough to search for A $\rightarrow \tau\tau$ in the high mass range (>∼100 GeV). An important test is of course to see the efficiency with which the experiments can record and reconstruct inclusive Z $\rightarrow \tau\tau$ events. This works rather well at the Tevatron with lower E_T thresholds.

6.5 A possible menu at LVL1

Table 2 illustrates the conditions one envisages to use in Atlas and CMS, at LVL1, to catch all the interesting high p_T physics. All of them use the signatures described above, namely electrons, photons,jets, τ-jets, E_T miss and some of their combinations.

Table 2: Examples of LVL1 trigger tables from ATLAS and CMS.

	ATLAS		CMS	
Trigger type	**Threshold (GeV)**	**Rate (kHz)**	**Threshold (GeV)**	**Rate (kHz)**
Inclusive isolated electron/photon	25	12.0	29	3.3
Di-electrons/di-photons	15	4.0	17	1.3
Inclusive isolated muon	20	0.8	14	2.7
Di-muons	6	0.2	3	0.9
Single τ-jet trigger	—	—	86	2.2
Two τ-jets	—	—	59	1.0
τ-jet $* E_T^{miss}$	$25 * 30$	2.0	—	—
1-jet, 3-jets, 4-jets	200, 90, 65	0.6	177, 86, 70	3.0
Jet $* E_T^{miss}$	$60 * 60$	0.4	$88 * 46$	2.3
Electron * Jet	—	—	$21 * 45$	0.8
Electron * Muon	15 *10	0.1	—	—
Minimum bias (calibration)			none	0.9
Others (monitor, calibration, etc.)		5.0	—	—
Total		25		16

The differences in estimated rates in the two experiments can be related to differences in their layouts and trigger thresholds.

6.6 W and Z for calibration and Standard Model Physics measurements

From cross-section, acceptance ($\eta < 2.5$) and trigger efficiencies, one calculates event rates for a given luminosity. Assuming 100 days at a peak luminosity of 2 10^{33}, one gets:

- 5 10^6 Z $\rightarrow$ ee and 5 10^6 Z $\rightarrow \mu\mu$ to mass storage (0.5 Hz each)
- 5 10^7 W $\rightarrow e\nu$ and 5 10^7 W $\rightarrow \mu\nu$

- Using the Z mass constraint ($m_Z = 91188 \pm 2$ MeV) one can
  - fix the EM calorimeter and the muon spectrometer scales
  - measure the W mass to ~15 MeV/expt (presently $m_W = 80403 \pm 29$ MeV from the combination of several experiments) using isolated leptons + E_T miss events to obtain an important constraint on the standard model (see below)
  - calibrate the jet scale using Z+jet events and γ+jet events (using p_T balance)

It is may be useful to recall that:

- no inclusive Z $\rightarrow$ jet-jet nor W $\rightarrow$ jet-jet samples can be isolated due to overwhelming background. However, top quarks are a source of Ws (see below)
- From WW, WZ, Zγ, ZZ,... in the final sate, one can determine triple Gauge bosons couplings and probe the standard model.

7 b-tagging, top quark identification

7.1 Vertex detectors specifications

Requirements on the vertex detectors are based on b-jets parameters: the B-hadrons lifetime is in average 1.6 ps to which corresponds $c\tau = 470$ μm meaning, for the decay particles of the B-hadron a (Lorentz boost invariant) impact parameter d $\sim$100 μm (see figure 36).

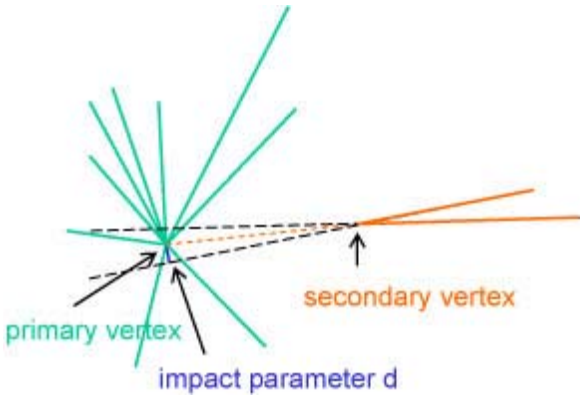

Figure 36: Impact parameter definition.

In order to measure d in a relevant way, an accuracy of $\sim$20 μm is necessary.

The main limitations to the accuracy of the measurement from a dedicated detector located around the vertex are the granularity, the lever arm and the number of layers.

The solution retained by both Atlas and CMS is a 3 layer pixel detector, with the first layer as close as possible to the beam pipe (5cm radius), a single hit accuracy of 15 microns in rϕ, equipped with fast electronics. The most difficult challenge posed by this detector is the radiation resistance of both the sensors and the electronics. This being solved, the other main difficulties are the power dissipation, the associated cooling and the transparency (conversions, multiple scattering).

While optimised for b-tagging, the vertex detectors play an important role for τ-physics.

7.2 The Atlas pixel detector[18]

The Atlas pixel detector features 3 cylinders of radii 5cm, 10cm and 13cm complemented by 2×3 disks. To withstand the radiation fluence in the best possible way, the Silicon detectors are of the "n + n oxygenated" type, with a pixel granularity of 50×400 μm. The front-end electronics is realized in a 250 nm IBM CMOS technology. The cooling is evaporative. In total, each pixel layer (without the piping and cabling) represents $0.028X_0$. In total there are 80 millions of electronics channels, each featuring a bump bonding to the sensor, a low noise preamplifier (200 electrons rms) giving an excellent signal/noise ratio (signal $\sim$15000 electrons before irradiation) and a discriminator. Since the occupancy is small ($<<$%), the readout proceeds by columns, each FE chip covering 24 columns of 160 cells [400×50 μm] ie $\sim$1cm^2.

Schematically, the "End of Column logic" drains data from columns which consist in the address of the hit pixel(s) in the column and a collision bunch counter. Upon a LVL1 request (which comes with a bc stamp) a microcontroller scans over its associated FEchips ($\sim$12), gather the hit pixel adresses +bc, keeps those with proper bc,and clears the buffers.

7.3 Expected tagging performance

In Atlas the reconstruction starts from a calorimeter cluster (QCD jet or τ-jet). The track reconstruction proceeds, gathering hits from the pixels, the SCT and the TRT. Tracks above a certain p_T threshold ($\sim$ 1 GeV/c), and coming from close to a "main interaction vertex" in a cone ΔR<0.4 around the seed are selected. Removing the constraint that all tracks are coming from a common vertex, the impact parameter d (positive if the track crosses the line vertex-cluster center between these 2 points, negative otherwise) and its error σ are calculated, from which the significance s=d/σ is deduced (Fig. 37).

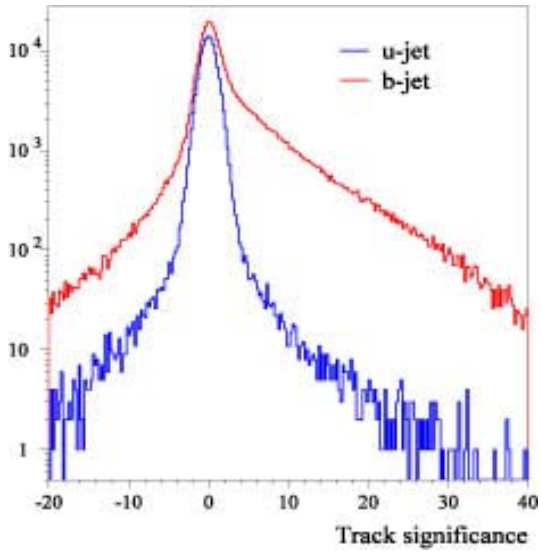

Figure 37: impact parameter significance for simulated jets.

The next steps are to calculate a jet weight as W=$\sum$log (significance) from all its tracks, and adjust a cut position depending on the physics channel under study.

Using B jet samples from a 100 GeV Higgs and a 400 GeV Higgs decaying in b$\bar{\text{b}}$, and background events from QCD jets in the same p_T range, one obtains the curves shown in Figure 38 (for L=2×10^{33}).

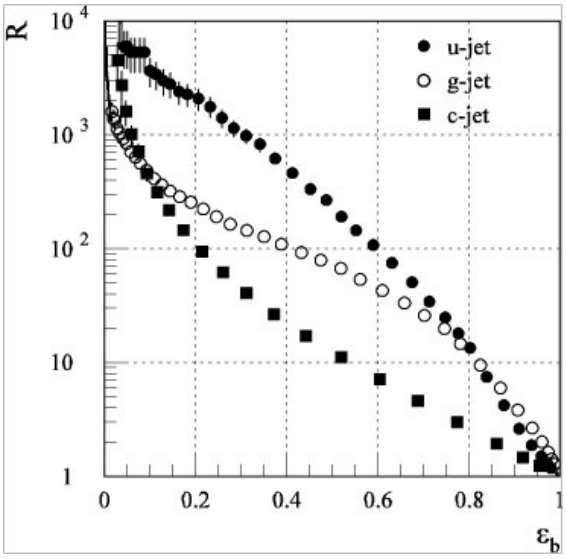

Figure 38: Light jet rejection as a function of b-jet acceptance.

The rejection of charm jets is more modest than for u jets because of the lifetime of charmed particles ($c\tau$ between 100 and 300 μm). The existence of gluon splitting in $c\bar{c}$ limits the rejection of associated jets.

On top of b-tagging, b-jets can be identified by their leptonic decay (branching ratio of 11% each).

For some physics channels, it may be advantageous to apply b-tagging already at the trigger level. At the Tevatron,CDF has shown this to be possible already at the equivalent of LVL2 (input rate of a few kHz). At LHC, events to be processed at LVL2 have in general several jets, making the process too time consuming. A "real tracking" is needed to decide if some of the jets are B-jets or not, and the efficient way to do it is at the HLT. CMS have studied this possibility, showing a rejection rate about 10 times less than with a fully offline optimized, aligned and calibrated detector. This can however be interesting in some cases, especially when several b-jets are expected in the events.

7.4 Particle identification for top quark physics

One of the most interesting parameters of the top quark is its mass, because being so large as compared to the other fermions masses it plays a dominant role in several one-loop effects. In particular M(W), M(top) and M(Higgs) are linked in the standard model (and its extensions) by

$$m(W) = \left(\frac{\pi \alpha_{em}}{\sqrt{2}\ G_F}\right)^{1/2} \frac{1}{sin\theta_W \sqrt{1-\Delta r}} \tag{5}$$

in which Δr is a function of M(top) and log(m_H). See figures 39 and 40.

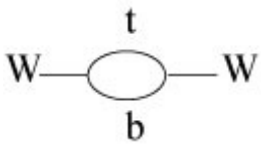

Figure 39: Loop diagram.

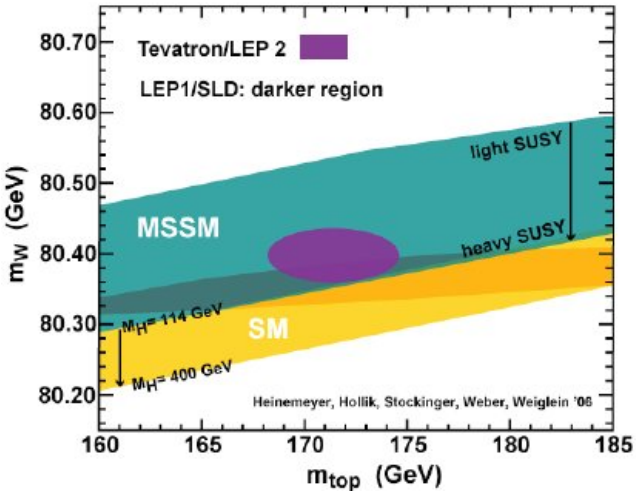

Figure 40: Relation between m_W, m_t, m_H.

G_F, α_{EM}, $\sin\theta_W$ being known with high precision, a precise measurement of M(top) and M(W) constrains M(H) (weakly because of the log term). Given the slope of the curve in figure 40, a precision of 15 MeV on M(W) corresponds to a precision of 2 GeV on M(top) [today, from the Tevatron, M(top) = 171.4 ± 2.1 GeV].

It is thus relevant to look for the best strategy-and in particular what is the best decay mode- to measure M(top) at the LHC, knowing that, given the expected high $t\bar{t}$ cross-section (0.7 nb, 100 times the Tevatron value) statistics will not be the problem.

Knowing that the top quark decays entirely in bW before hadronisation,and recalling that the W branching ratios to lepton-neutrino are 11% for each flavor, the rest (67%) being a hadronic 2-jet final state without bs, one has:

- W1→had, W2 → had: 44% 2 masses fully reconstructed, huge QCD BG
- W1→e$\nu/\mu\nu$, W2 → had (+ 2→1): 30% 1 mass fully reconstructed
- W1→e$\nu/\mu\nu$, W2 → e$\nu/\mu\nu$: 5%

Detailed simulations have shown that the semi-leptonic mode, which combines good identification through the leptonic mode, and full reconstruction through the hadronic decay of the second top, represents the best approach.

For 10fb^{-1}, 2.5 million events are produced in this mode, which combines several important features of particle ID at the trigger and analysis levels:

- one electron or muon → LVL1 lepton trigger
- two b jets → b-tagging
- two non-b-jets Minv=M(W) → jet mass scale by imposing m_W
- missing E_T → reconstruction of the 1/2 leptonic top mass

In addition a $t\bar{t}$ event will have (from QCD) in average 2 or 3 additional gluon jets and the soft particles of the "underlying event".

Quantitatively, the simulation of the selection criteria below

- 1 isolated lepton, $p_T > 20$ GeV, $|\eta| < 2.5$
- $E_T$miss > 20 GeV
- ≥ 4 jets with $p_T > 40$ GeV, $|\eta| < 2.5$
- ≥ 2 jets with b-tag

reduces the produced sample to 125 thousand events (ie a selection efficiency of 5%) with a signal/background ratio of ∼65. The invariant masses obtained by simulation are shown in figure 41 (from ATLAS).

One can remark that despite the high purity of the sample, some combinatorial background remains, due to either the imperfect b-tagging efficiency or/and the additional QCD jets.

The clean "W sample" is one of the important tools that the $t\bar{t}$ sample provides to the experiments, allowing an accurate calibration of non-b jets for a broad list of physics channels.

The calibration of b-jets, which enters directly in the top mass value needs to be established from a different source. One of them are the events Z + jets, where the jet is tagged as "b".

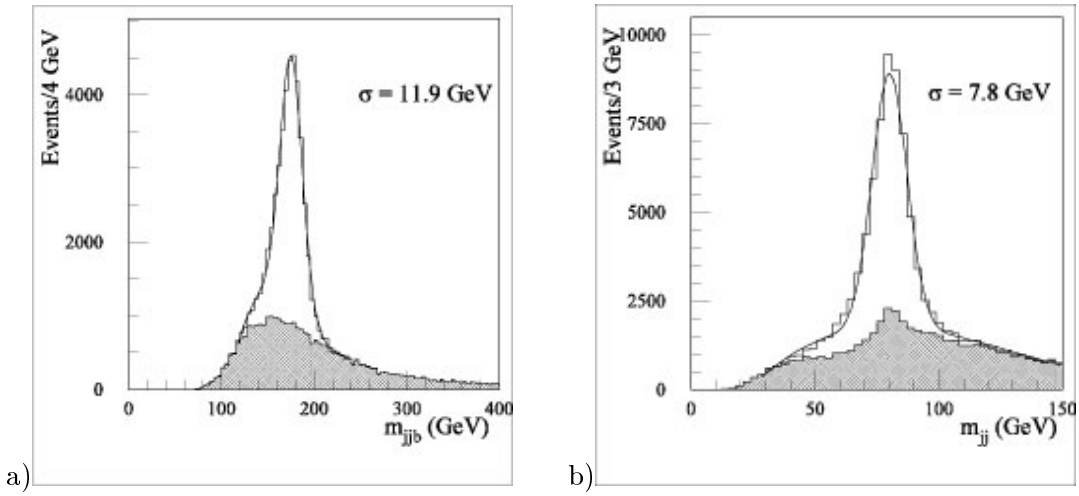

Figure 41: a) Fully reconstructed bjj top mass, b)jj mass of the intermediate W.

8 Particle identification for Higgs search and SUSY

8.1 Standard model Higgs search

The standard model has been so far extremely successful in describing all relevant particle physics data. However the cornerstone of it, namely the Higgs particle, still awaits discovery. This is an essential part of the LHC programme.

Given the LEP lower limit (114.4 GeV), and the constraints from existing precision measurements, the most likely range for the Higgs mass is between 114 and ∼300 GeV, while the LHC allows to search for it up to 1 TeV, above the presently accepted upper limit for its mass, from theory constraints.

Given the strongly varying branching ratios as recalled in figure 42, the strategy for Higgs search at the LHC depends strongly upon its mass. Because the production cross-section is small (at most a few tens of picobarns - see figure 43 for the dominant amplitudes), the discovery channels rest heavily on particle identification to resolve them from QCD background.

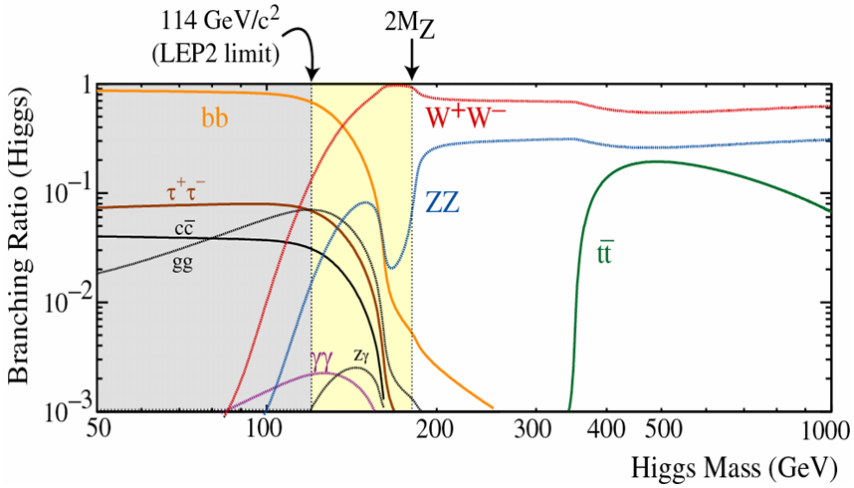

Figure 42: Higgs decay branching ratios.

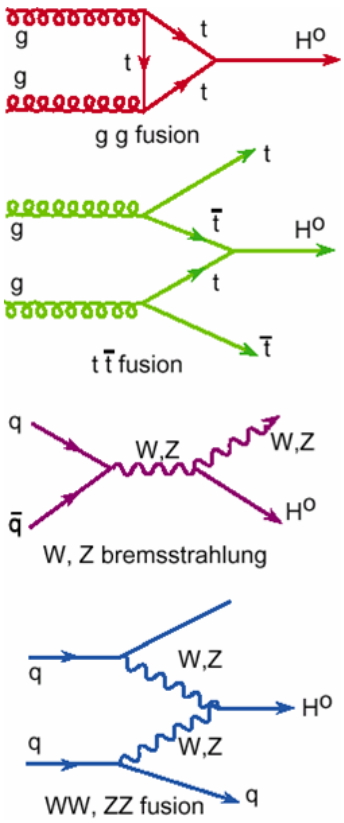

Figure 43: Graphs contributing to Higgs boson production.

Their potential significance is illustrated in figure 44 which shows that the 6 most significant of them require either photons, or leptons or b-tag in the final state, or a mixing of both. In the following we consider briefly some of these decay channels, concentrating on the particle identification aspects.

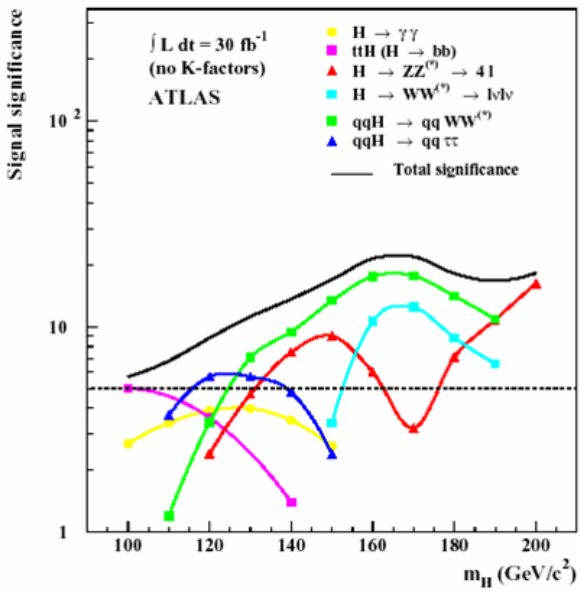

Figure 44: Main channels contributing to the Higgs search.

8.2 The ZZ and ZZ* modes

Above 180 GeV the ZZ mode is open, and constitutes, with 4 high p_T leptons in the final state and the two Z mass constraints the "golden mode" of Higgs search. The only background is the non-resonant ZZ channel, which is small as compared to the expected signal. With 10 fb^{-1} one expects (for M(H)=200 GeV) about 40 signal events, and a smooth background level under the peak of about 25 events, giving a signal significance ($S/\sqrt{B}$) of 8. The significance (see figure 44) stays ∼constant up to ∼500 GeV where it drops because of the decreasing production cross-section.

To go higher in mass,one tries to use the events in which one of the Zs goes to $\nu\nu$, taking advantage of a factor 3 in rate as compared to ee, $\mu\mu$ and eμ together. The signature of one leptonic Z plus missing E_T is indeed weaker than 2 physically observed Zs. This reaction is one of those which were used to define the angular coverage of the detectors, and extend it up to η=5. In principle this mode extends the sensitivity up to M(H)≃700 GeV.

Another question is to explore if the ZZ mode, with one Z decaying hadronically (in $b\bar{b}$ to reduce the QCD background), can improve the sensitivity. This is the pedagogical example taken at the beginning. This was looked at, with a rather negative answer due to an unfavourable signal/background ratio (Z + 2 jets with $p_T > 50$ GeV has a too high cross-section...).

Coming back to the 4 leptons final state,one can explore lower masses, potentially very interesting given the known constraints on M(H), if one accepts that one of the Z is off mass shell. Indeed one loses in this way one mass constraint, and one needs also to accept leptons with lower p_T. Since there are 4 leptons in the final state, it is enough that 2 are at high p_T to give the trigger, while the other two may be found only off-line. In Atlas it is estimated that the lower limit for reliable electron-id (off-line) is 7 GeV/c.

Due to the loss of the second M(Z) constraint, the channel Zb$\bar{b}$ gives a non negligible background,which can be reduced by asking that the two low energy electrons do come from the main vertex, and not from a detached one ("anti tagging"). The sensitivity obtained by simulating all these features is shown by the low mass part of the red curve in figure 46. The drop of sensitivity around 170 GeV is due to the opening of the on-shell WW decay.

8.3 The $\gamma\gamma$ mode

This decay mode, one of the most promising in the low M(H) range, combines several negative features: a limited σ BR,a large irreducible background and potentially a large instrumental background (jet-jet and γ-jet), compensated however by a clean signature and a high invariant mass resolution. The $\gamma\gamma$ mode served as bench mark for the electromagnetic calorimeters definition (see section 5). When all calibration problems are solved, the ultimate energy resolution expected for unconverted photons is:

- CMS: $3\%/\sqrt{E} \oplus$ (200 MeV ⊕ pile-up)/E ⊕ 0.55%
- ATLAS: $10\%/\sqrt{E} \oplus$ (200 MeV ⊕ pile-up)/E ⊕ 0.70%

A Higgs mass resolution of ∼1% is the (difficult) target, together with large acceptance (up to $\eta = \pm 2.5$), high trigger and reconstruction efficiency, and efficient background rejection.

Figure 45, from CMS shows the various contributions to the $\gamma\gamma$ spectrum, signal and backgrounds. The different colours allow to distinguish the irreducible from the different sources of reducible background. With 30fb^{-1} and a simple "cut based" analysis, a significance of 5 σ is expected for M(H)=120 GeV. For Atlas the expected end result is similar when k-factors are introduced (see figure 44 -without k-factors) the somewhat worse mass resolution being compensated by a better jet background rejection. One should also remember that if the vertex position along z is unknown, like it is going to be for most $\gamma\gamma$ events at 10^{34} luminosity, the

mass resolution worsens by an additional ∼1.3 GeV. In this case the direction measurement in the Atlas calorimeter, and the use of converted photons in both experiments (for once) help reducing this contribution.

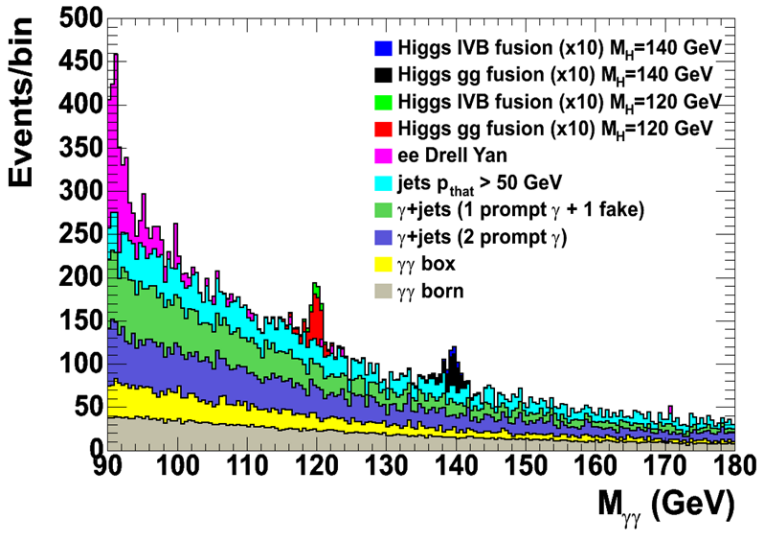

Figure 45: Two photons mass spectrum in CMS.

In both cases more sophisticated analysis tools taking into account the kinematic characteristics of the signal and of the various backgrounds carry the potential of getting this same significance with less luminosity (the same is actually true for most if not all the decay channels considered here).

8.4 The Higgs $\to \tau\tau$ by Vector Boson Fusion

The $\tau\tau$ mode has a larger branching ratio than $\gamma\gamma$ (factor ∼20 at production, somewhat less after trigger) but a weaker signature and a worse mass resolution.

A promising approach is to ask for 2 forward jets (and no further central jet) in order to selects the weak process by WW fusion, which has less background than inclusive Higgs production.

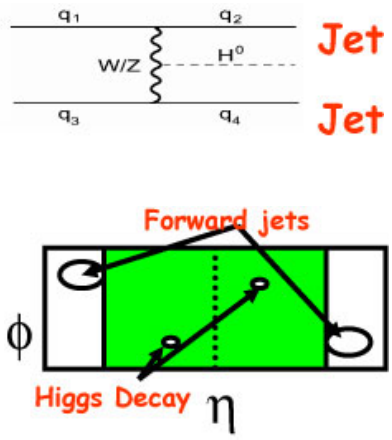

Figure 46: Characteristics of H production by VBF.

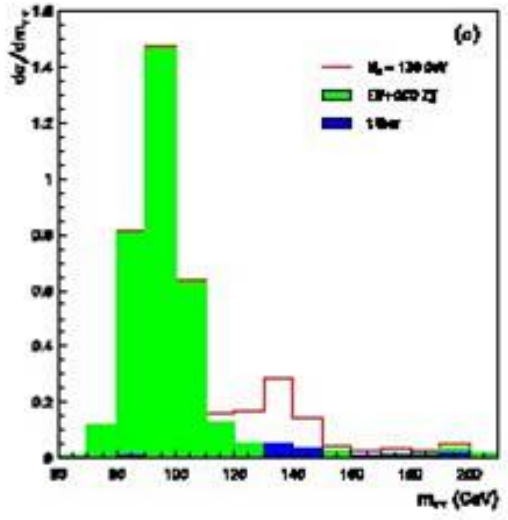

Figure 47: $\tau\tau$ invariant mass in VBF.

In Atlas, in order to catch a large fraction of those events, it is envisaged to use 3 trigger conditions in parallel:

- dilepton (E15mu10)
- lepton-hadron ($p_T$lept $>$ 20 GeV)
- τ-jet plus missing E_T (Tau35 x MET45)

On top of verifying offline the trigger conditions, the analysis requires 2 "tagging jets" with a difference in pseudo rapidity >4, and M(JJ)$>$700 GeV.

Detailed simulation of signals and backgrounds shows that the dominant ones are $t\bar{t}$ and Z+2 jets events.

The $\tau\tau$ invariant mass is calculated using their lepton/hadron visible decay particles and jets, plus $E_T$miss as explained in section 6.4. An example of invariant mass plot is given by figure 47 in the case of Atlas, for 30 fb^{-1} and the associated significance is given in figure 45.

The question of "jet-tagging" not discussed so far is a difficult one. From the kinematics and dynamics of the reaction, the jets signing VBF are concentrated in the region of pseudo rapidity between 2 and 4, in which the QCD background is high. When luminosity increases there is a risk of accidental coincidences between single forward jets on each side, as well as of mis-measurement due to pile-up. The quantity of interest is actually the transverse energy of the jets, more than the energy itself, which calls for high granularity of the calorimeters in this η region. In order to satisfy these requirements, CMS decided to recess their very forward calorimeters at 11 m from the interaction point, which creates a discontinuity with the rest of the calorimetry. In Atlas it is located in the end cap cryostat, at $\sim$5m from the vertex. The coverage is continuous, but the radiation fluence is very high(up to 10^{17} n/cm^2); in principle liquid argon should survive here...

8.5 A glance at super symmetry

In super symmetry each fermion $f_{L,R}$ has a scalar partner $\tilde{f}_{L,R}$, and to each Gauge boson is associated a massless spin 1/2 gaugino.

Among other virtues, these states coming with an opposite sign to normal particles in loop corrections, cancel the quadratic divergence of the Higgs mass, which would otherwise run to "infinity".

None of the s-particles has been observed so far. Thus they should be heavy, and the super symmetry is a broken symmetry.

$\tilde{q}$ and $\tilde{g}$ couple to QCD as usual particles: they should thus be copiously produced at LHC as soon as threshold is passed.

In the Minimum super symmetric model R-parity = $(-1)^{3(B-L)+2S}$ is conserved, which insures that:

- s-particles are produced in pairs
- the lightest one is stable: it is usually one of the mixed neutral gauginos, the neutralino χ_1^0

Exact signatures depend on the details of the model, however a common feature is large $\sum E_T$ and large $E_T$miss (the neutralinos escape the detector like neutrinos).

The reach of experiments can be evaluated and compared to models using as parameter m_0 ($m_{1/2}$) the common mass of all scalars (spin 1/2) at GUT scale. This is illustrated in figure 48 in the case of CMS. The rates are high, and in principle, in one month at 10^{33}cm^{-2}s^{-1}, s-quarks and gluinos up to ∼2 TeV can be discovered. The main background is Z→ $\nu\nu$ +N jets. Its evaluation is still subject to improvements in the framework of NLO QCD calculations.

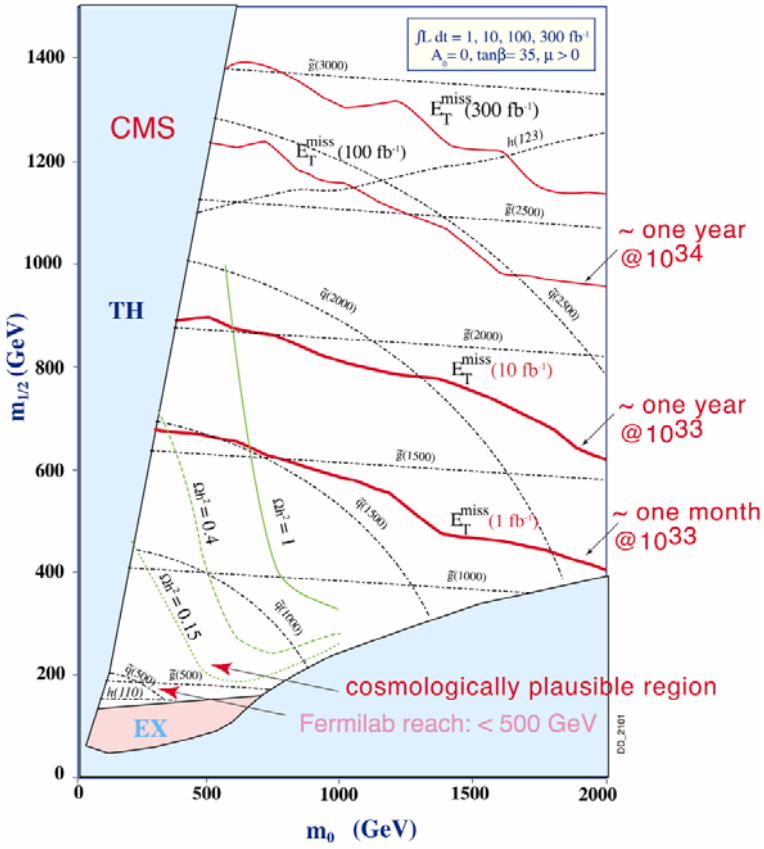

Figure 48: SUSY discovery potential of CMS.

Once super symmetry is discovered (if ...), a full new program starts, with the search for cascade decay chains which may allow to measure the mass of the lightest neutralino(χ_1^0), and

to go back to some of the fundamental parameters of the underlying theory. In such a program leptons play again a prominent role, both in allowing to select the cascade decays from background, and in giving accurate measurements of end points in decay spectra.

An example is depicted in figure 49. Measurements of the $(ll)_{max}$, $(l^{\pm}j)_{max}$, $(llj)_{max}$ and $(llj)_{min}$ values of the spectra allow in the chosen example (so called SPS point 5) to measure the χ_1^0 mass with an accuracy of about 12%.

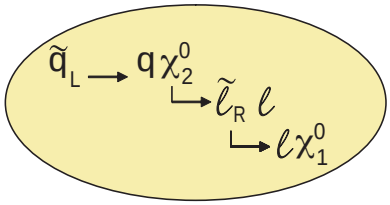

Figure 49: An example of SUSY decay chain.

In the MSSM, there are 5 Higgs bosons (h, H, A, $H^{\pm}$), whose masses are function of 2 parameters, usually taken as M(A) and tg(β). When tg(β) is large, the coupling of H, A to τ pairs is enlarged. This decay mode is among the most proming ones for Higgs search in this scenario.

9 Summary and Conclusions

The two specialized experiments, Alice for heavy ion collisions, and LHCb for B physics are making use of specific techniques adapted to their physics program, for which identification of particles at low p_T (but high momentum in the case of LHCb) is important. This includes Time of Flight, Cerenkov and Transition Radiation detectors, as well as calorimetry and muon detection.

For the physics program of the general purpose detectors, Atlas and CMS, the challenges raised by hermiticity, precision calorimetry, precision muon detection, b-tagging, tau identification,... are even higher.

It is remarkable that the two detectors are complementary in several critical aspects, with in particular crystals against liquid argon for their electromagnetic calorimetry, and toroids against solenoid for their muon spectrometer,...

Both of them share an extremely challenging pixel vertex detector, and a multilevel trigger system.

The performance of each of them will depend critically upon these choices, but also on the quality and the flexibility of their online and offline Software.

In a year or two the community will see how well each of them manages with the first data, hopefully rich of new physics.

Acknowledgements:

It is a pleasure to thank the organizers of the meeting in El Escurial. In writing these proceedings I have benefited a lot of the competent contribution of Mrs Catherine Bourge. I also thank Françoise Maréchal for reading the manuscript. It goes without saying that the material discussed here exists only thanks to the hard work of hundreds of scientists and technicians embarked since many years in the LHC program.

References

[1] LHC Technical Design Report - Vol. I (1996) and LHC Conceptual Report CERN/AC/95-05 (1995

[2] H.L. Lai et al, Eur. Phys. J. C. 12 (2000) 375
J. Pumplin et al., hep-ph/0201195 (2002)

[3] ALICE Technical Proposal, CERN/LHCC/95-71 (dec 1995)

[4] Extensive particle identification with TPC and TOF at the STAR experiment. M. Shao et al., NIMA 558 (2006) 419

[5] Observation of $B - \bar{B}$ oscillations - CDF Collaboration, PRL97 (2006) 242003

[6] LHCb Technical Proposal, CERN/LHCC 98-4

[7] Performance Study of Hybrid Photon Detectors for the LHCb Rich, NIMA 553 (2005) 41

[8] B. Anderson et al., Parton fragmentation and string dynamics, Physics Report 97 (1983) 31

[9] Review of Particle properties - Passage of particles through matter, Phys. Lett. B 592 (2004)

[10] ATLAS Coll., ATLAS Tech. Propos. CERN/LHCC/94-43 (1994); CMS Collab., CMS Tech. Propos. CERN/LHCC/94-38 (1994)

[11] ATLAS Collab., Muon Spectrom. Tech. Design Report, CERN/LHCC/97-22 (1997); CMS Collab., Muon Proj. Tech. Design Report, CERN/LHCC/97-32 (1997)

[12] ATLAS Collab., Level-1 Trigger Tech. Design Report, CERN/ LHCC/98-14 (1998); ATLAS Collab., High level Trigger, Data Acquis. Controls Tech. Design Report, CERN/LHCC/2003-022 (2003)

[13] CMS Collab., triDAS Proj. Tech. Design Report Vol. I: The trigger systems, CERN/LHCC/2000-38 (2000); CMS Collab., triDAS Proj. Tech. Design Report Vol. II: Data Acquisition and High-level trigger, CERN/LHCC/2002-26 (2002)

[14] CMS Collab., Electromagn. Calorimeter Tech. Design Report, CERN/LHCC/97-33 (1997)

[15] ATLAS Collab., Liq. Argon Calorimeter Tech. Design Report, CERN/LHCC/96-41 (1996)

[16] Uniformity of the ATLAS electromagnetic calorimeter. Submit. to NIM

[17] Linearity and resolution of the ATLAS electromagnetic barrel calorimeter NIMA 568 (2006) 601

[18] ATLAS Collab., Pixel Detect. Tech. Design Report, CERN/LHCC/98-13 (1998)

[19] Position resolution and particle identification with the ATLAS EM calorimeter, NIMA 550 (2005) 96

[20] ATLAS Collab., ATLAS Tile Calorimeter Tech. Design Report, CERN/LHCC/96-42 (1996); CMS Collab., Hadron Calorimeter Proj. Tech. Design Report, CERN/LHCC/97-31 (1997)

[21] An improved τ identification for ATLAS. M. Heldmann and D. Cavalli, ATLAS note ATL-PHYS-PUB-2006-009

[22] CMS Collab., Tracker Proj. Tech. Design Report, CERN/LHCC/98-6 (1998)

[23] ATLAS Collab., Detect. Phys. Perform. Tech. Design Report, CERN/LHCC/99-15 (1999)

[24] CMS Collab., Physics TDR, CERN/LHHC/2006-001 and CERN/LHCC/2006-021